Inorganic Chemistry

Open Access

pubs.acs.org/IC

Article

Speciation of Chlorido Complexes of Rhodium(III) in Ethylene Glycol

Vincent Cool, Gert Steurs, Iztok Arčon, Sofía Riaño, Tom Van Gerven, and Koen Binnemans*

Cite This: https://doi.org/10.1021/acs.inorgchem.5c02591

Read Online

ACCESS | Metrics & More | Article Recommendations | Supporting Information

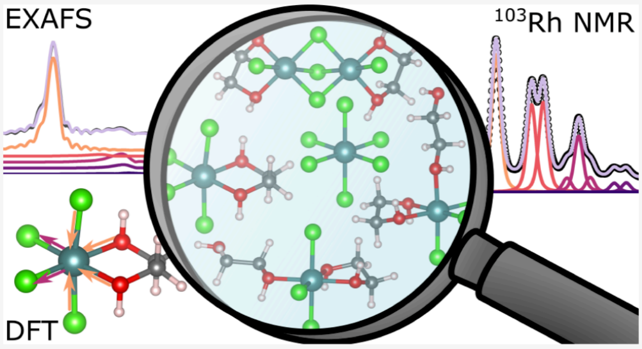

ABSTRACT: The speciation of rhodium(III) chlorido complexes was investigated in ethylene glycol, in the presence and absence of lithium chloride, by rhodium-103 NMR and EXAFS spectroscopy. All major rhodium(III) complexes were identified based on their species-specific isotopologue and isotopomer patterns. EXAFS analysis confirmed the results deduced from the rhodium-103 NMR spectra. The strikingly different shifting behavior observed with increasing lithium chloride concentration was linked to the established behavior of rhodium(III) in NMR spectroscopy. Density functional theory (DFT) calculations were performed to elucidate the underlying factors of the observed trends, highlighting their potential as an additional tool for the speciation of rhodium(III) complexes, even for NMR spectra with a low signal-to-noise ratio. These results give a deeper insight into the speciation of rhodium(III) in a nonaqueous environment and contribute to the fundamental basis needed to understand the extraction behavior of rhodium(III) in nonaqueous solvent extraction.

1. INTRODUCTION

The high demand for rhodium as a versatile catalyst in the chemical industry[1] and in automotive exhaust catalysts,[2] in combination with its scarcity and its production solely as a byproduct in platinum and nickel/copper ores,[3,4] has made it one of the most expensive metals.[5−8] A variety of hydrometallurgical flowsheets have been proposed to purify rhodium from platinum group metal (PGM) feeds, accompanied by numerous studies aimed at unraveling rhodium's complex chemical behavior in aqueous solutions.[9−15] While a general consensus on rhodium's aqueous behavior can be drawn from extensive research studies, its speciation in organic solvents has received much less attention. Combined with the lack of solvent extraction studies in nonaqueous media such as deep-eutectic solvents (DESs), ionic liquids (ILs), and polar organic solvents, this limited knowledge of the nonaqueous coordination chemistry of rhodium has hampered the development of promising solvometallurgical alternatives to existing hydrometallurgical extraction methods.[16]

Nonaqueous solvent extraction (NASX), involving two immiscible nonaqueous solvents, has been demonstrated for purifying rare earths and the 3d transition metals but has not often been applied to PGM flowsheets.[17−19] Nguyen et al. demonstrated the separation of iron, palladium, and rhodium by an NASX system comprising an ethylene glycol feed solution and the quaternary ammonium extractant Aliquat 336.[20] This study is primarily focused on leaching behavior and does not give insight into the speciation in the two immiscible organic phases.

High-resolution rhodium-103 nuclear magnetic resonance spectroscopy (^{103}Rh NMR) is a valuable tool for the identification and characterization of rhodium(III) complexes. Rhodium-103 is a spin-1/2 nucleus with 100% natural abundance. Its corresponding advantages are largely negated by its low gyromagnetic ratio ($\gamma = -0.8468 \times 10^7$ rad·T^{-1}·s^{-1}), complicating probe tuning and causing acoustic ringing, difficult excitation (necessitating short, high-power pulses due to large spectral width), and low receptivity. In the early studies by Mann et al.[21] and Fedotov et al.,[22] several rhodium(III) aqua−chlorido complexes were identified based on relative chemical shifts, but the authors failed to distinguish the different structural isomers (*fac*/*mer* and *cis*/*trans*). Later, Carr et al. acquired all 10 rhodium aqua−chlorido complexes and revised their NMR resonance assignments.[23] Furthermore, this study laid the foundation for the identification of rhodium(III) complexes through the use of secondary isotope effects, as illustrated by the observed isotope pattern of the *cis*-$[RhCl_4(OH_2)_2]^-$ complex.

The high sensitivity of ^{103}Rh NMR spectra to temperature, concentration, and solvation makes a comparison of the different experimental and literature data difficult. This is illustrated by the $[RhCl_6]^{3-}$ complex, for which changes in

Received: June 6, 2025
Revised: July 19, 2025
Accepted: August 6, 2025

chemical shifts of ±129 ppm are observed in aqueous solutions. Hence, the chemical shift in ^{103}Rh NMR spectra is not a reliable tool for the identification of rhodium(III) complexes. A much more powerful tool for the unambiguous identification of rhodium(III) complexes is the "fingerprint" method based on the observed secondary isotope effects, which was first described by Carr et al. for the *cis*-$[RhCl_4(OH_2)_2]^-$ complex and further developed by Geswindt et al.[15,23]

These secondary isotope effects, while particularly useful for determining the number of chlorido ligands surrounding a rhodium(III) ion, are typically too small and often remain undetectable in the NMR spectra of d-block metals. Rhodium, however, is particularly well-suited for observing such fine structure as a result of its narrow resonance peaks, even in asymmetric environments. Nevertheless, ^{103}Rh NMR is hardly a routine method and needs a specialized low-frequency NMR probe, while its low receptivity further limits its applicability.[24] Indirect detection pulse sequences were developed to circumvent these issues but require a spin-coupled nucleus with spin = 1/2, high γ, and high natural abundance (or isotopically enriched samples).[25−29] These requirements significantly reduce their applicability and cannot be fulfilled by the aqua−chlorido complexes investigated in this study. Hence, the described "fingerprint" method is limited to identifying the most abundant complexes and requires the use of concentrated ($\geq$0.4 mol·L^{-1}) rhodium solutions.

Despite the large discrepancies in chemical shifts for ^{103}Rh resonances reported in the literature, relative chemical shifts remain useful in significantly narrowing down the number of plausible species or, in some cases, even identifying the complexes. The relative chemical shift avoids the necessity of acquiring ^{103}Rh NMR spectra with a high signal-to-noise (S/N) ratio, which, due to its low gyromagnetic ratio, is not straightforward or even practically feasible.

In this paper, all major and several minor observable rhodium(III) chlorido species are identified in ethylene glycol solutions with LiCl concentrations ranging from 0 mol·L^{-1} to 3.346 mol·L^{-1} by direct ^{103}Rh NMR spectroscopy, based on three key aspects: (1) relative chemical shifts, (2) isotopologue patterns caused by the secondary isotope effect of the chlorido ligands, and (3) isotopomer patterns (*cis*/*trans*; *fac*/*mer*). The identification of $[RhCl_6]^{3-}$ and *cis*-$[RhCl_4(\kappa^2\text{-EG})]^-$ complexes by ^{103}Rh NMR spectroscopy is confirmed by extended X-ray absorption fine structure (EXAFS) spectroscopy, and the formation of hypothetical dirhodium(III) species is refuted. A strong, species-specific dependency of the chemical shift of ^{103}Rh as a function of the LiCl concentration is identified and elucidated by density functional theory (DFT) calculations.

2. EXPERIMENTAL SECTION

2.1. Products. Rhodium(III) chloride hydrate ($RhCl_3\cdot xH_2O$, 39.68% w/w Rh) was received from Johnson Matthey (United Kingdom). Ethylene glycol ($\geq$99.5%) was purchased from Supelco (Darmstadt, Germany). Lithium chloride (LiCl, 99%), deuterium oxide (D_2O, 99.9 at % D), nitric acid concentrate (0.1 mol·L^{-1} HNO_3; eluent for IC), and 2,6-pyridinedicarboxylic acid (99%) were obtained from Sigma-Aldrich (Overijse, Belgium). Triton X-100 was purchased from Merck KGaA (Darmstadt, Germany). A silicone solution in isopropyl alcohol was obtained from SERVA Electrophoresis GmbH (Heidelberg, Germany). Ethanol (99.8%) was purchased from Fisher Scientific (Loughborough, United Kingdom). 1000 mg·L^{-1} standard solutions of palladium (Plasma HIQU) and lithium (Ion HIQU) were obtained from Chem-Lab nv (Zedelgem, Belgium). Ultrapure water (18.2 MΩ·cm) was produced using a Merck Millipore Milli-Q Reference Ultrapure Water Purification System. All products were used as received without any further purification.

2.2. Rhodium Solutions. Five solutions containing approximately 0.42 mol·L^{-1} Rh (Supporting Information,Table S1) were prepared with varying concentrations of lithium chloride (0.0, 0.154, 0.514, 2.541, 3.346 mol·L^{-1} LiCl) in ethylene glycol. The final rhodium concentration in each solution was measured using a Bruker S4 T-STAR 400 Plus total reflection X-ray fluorescence (TXRF) spectrometer equipped with a tungsten X-ray source. All measurements were performed by using a voltage of 50 kV and an electrical current of 1000 μA.

Each solution was diluted a total of 625 times in two steps prior to TXRF analysis. First, a 25-fold dilution was performed using ultrapure water. Second, an additional 25-fold dilution was performed with a 5 vol % Triton X-100 solution in ethanol. Twenty vol % of ethylene glycol and 50 mg·L^{-1} palladium (final concentration) were added to ensure the formation of a smooth film during drying and for the calibration of rhodium, respectively. Measurements were performed on reusable quartz glass sample carriers, pretreated with 30 μL of silicone solution in isopropanol (SERVA) and left open to dry for 30 min. Two μL of the final solution in ethanol was pipetted onto the pretreated carriers and dried for 30 min in a hot air oven at 60 °C. Gain corrections were performed prior to all measurements.

The final LiCl concentration was measured by ion chromatography (IC) with a Shimadzu chromatograph equipped with a CBM-40 system controller, SIL-20A pump, SIL-20A autosampler, CTO-40C column oven, DGU-403 degassing unit, CDD-10AVP conductivity detector, and Metrosep C4-250/4.0 cation column. All samples were diluted with ultrapure water. A 1.7 mmol·L^{-1} nitric acid and 0.7 mmol·L^{-1} pyridine-2,6-dicarboxylic acid solution in ultrapure water was used as the eluent. A temperature of 25 °C and a flow rate of 0.9 mL·min^{-1} was used throughout.

The water content of the ethylene glycol solutions was determined by Karl Fischer titration using a Mettler-Toledo C30S coulometric titrator with the HYDRANAL-Coulomat AG analyte (Table S2).

No uncommon hazards were noted during the preparation and handling of the rhodium solutions.

2.3. Rhodium-103 NMR Spectroscopy. ^{103}Rh NMR spectra were recorded on a Bruker Avance Neo 600 spectrometer with a Bruker Ascend 600 magnet system fitted with a 10 mm PABBO BBLR (^{41}K−^{97}Mo)-1H/D custom probe with z-gradients and an ATM accessory for automatic tuning and matching. Data acquisition and processing were performed using Topspin 4.4.1 software. All experiments were performed using Bruker's standard aring pulse sequence to minimize acoustic ringing. Measurements were performed in Norell Standard Series 10 mm NMR tubes containing a custom reference tube, with an outer diameter of 1.58 ± 0.02 mm and an inner diameter of 1.24 ± 0.02 mm, inserted in the center. Samples were measured at 297.08 K, and a relaxation delay time of 10 s was used throughout. Before NMR analysis, all solutions except for the 0.514 mol·L^{-1} LiCl solution were aged for one month at room temperature (21 ± 1 °C). The 0.514 mol·L^{-1} LiCl solution was analyzed after only 48 h.

The lack of a universally accepted and widely used reference species is a key issue in ^{103}Rh NMR spectroscopy. Although saturated rhodium(III) acetylacetonate ($Rh(acac)_3$) in deuterated chloroform is recommended by the IUPAC,[30] its high T_1 delay time makes it inconvenient, and hence, this reference compound finds nowadays only limited use in ^{103}Rh NMR studies. The extensive chemical shift range in the ^{103}Rh NMR spectra further complicates the use of a single reference species. A less common approach, similar to what is commonplace for ^{183}W and $^{14/15}$N NMR spectra, would involve using several reference species, each suited for a specific shift range in the ^{103}Rh NMR spectra.[30−32] This practice is generally discouraged as it hampers seamless comparison across studies. To circumvent these inconveniences, many ^{103}Rh NMR studies adopt the referencing method proposed by Kidd and Goodfellow, which is based on the Ξ value of 3.16 MHz.[33] The proposed method can indeed alleviate the mentioned inconveniences by referencing a fixed frequency. Unfortunately, Ξ = 3.16 MHz was chosen arbitrarily, rather than representing the actual Ξ value for ^{103}Rh (Ξ = 3.186447 MHz),[30] which is defined as the ratio of the resonance frequencies of the nucleus of interest (IUPAC reference, $Rh(acac)_3$) to the resonance frequency of protons (tetramethylsilane).[34] This reference technique in turn requires careful recalibration if the NMR data are compared with other literature data that do not use the same arbitrary frequency of 3.16 MHz (eq S1).

To avoid introducing an additional chemical shift scale and to maintain consistency in NMR referencing, the recommended IUPAC reference scale was adopted throughout. For this, the tabulated Ξ value for ^{103}Rh (3.186447 MHz) was used to determine the chemical shift of the *cis*-$[Rh^{35}Cl_4(H_2O)_2]^-$ isotopologue. A deuterated (D_2O) solution containing 0.443 $mol\cdot L^{-1}$ $RhCl_3\cdot xH_2O$ was used as the reference solution, ensuring both the calibration of the spectra and the locking of the magnetic field. The determined chemical shift of the *cis*-$[Rh^{35}Cl_4(H_2O)_2]^-$ isotopologue (163.05 ppm) was applied to all of the spectra. The authors do, however, also recognize the widespread use of the alternative referencing method proposed by Kidd and Goodfellow. Therefore, identical figures with the alternative referencing method are added (Figures S1−S8).

An additional comment regarding the chemical shift of the rhodium(III) species is required. The isotopologue and isotopomer effects result in the formation of peak patterns which cannot be described by normal splitting patterns caused by *J*-coupling. Hence, the patterns cannot be characterized by a single chemical shift but rather by a range of chemical shifts for each isotopomer. Unless stated otherwise, the chemical shift of a peak pattern will be identified using the chemical shift of the $[Rh^{35}Cl_x{}^{37}Cl_0Y]^z$ isotopologue, which is the highest-frequency isotopomer.

It is well established that the Fourier transform of the free induction decay theoretically results in Lorentzian peaks.[35,36] However, the signals can deviate significantly from pure Lorentzian peaks due to broadening effects caused by imperfect shimming, field inhomogeneities caused by external factors, and temperature fluctuations. When the broadening effects are random in nature, the NMR resonances are broadened with a Gaussian function. Consequently, a Voigt function is more suitable for the deconvolution of the obtained ^{103}Rh NMR spectra.[37]

^{103}Rh NMR peak patterns were deconvolved using the nonlinear curve-fitting tool available in Origin 2018b (OriginLab Corporation), employing the Levenberg−Marquardt iteration algorithm. To restrict the number of parameters and allow robust deconvolution, the Gaussian and Lorentzian widths were treated as shared parameters. The position (chemical shift) and area of the peaks were iteratively optimized without further restrictions, unless mentioned otherwise.

2.4. XAS Spectroscopy. X-ray absorption spectroscopy (XAS) spectra of the 0.154 and 3.346 $mol\cdot L^{-1}$ LiCl solutions (*vide supra*), in the range of the rhodium K-edge (23220 eV), were collected at the P65 beamline of the PETRA III storage ring at Deutsches Elektronen-Synchrotron (DESY) in Hamburg, Germany.[38] A Si(311) double-crystal monochromator was used with an energy resolution of about 2 eV at 23 keV. The beam size on the sample was 0.3 × 1 mm. Higher-order harmonics were eliminated by using flat platinum-coated mirrors. The XAS spectra were measured at room temperature in transmission detection mode using three consecutive 5 cm-long ionization chambers filled with krypton at 1 bar. Samples with an optimal absorption thickness of about 2.0 were prepared in a custom 3D-printed sample holder with Kapton windows, inserted between the first and second ionization chambers (Figure S9).

The absorption spectra were measured from −150 eV to +1000 eV relative to the rhodium K-edge energy in continuous detection mode during short 3 min scans. The exact energy calibration was established through absorption measurements on a 5-μm-thick rhodium metal foil placed between the second and third ionization detectors. The absolute energy reproducibility of the measured spectra was ±0.05 eV.

The quantitative analysis of the rhodium K-edge EXAFS spectra to detect local structure was performed using the LARIX program package.[39] *Ab initio* calculations of the photoelectron scattering paths were calculated with the FEFF8 program code integrated into the LARIX software.[40,41] Structural parameters of the average local rhodium neighborhood (type and average number of neighbors, the radii, and Debye−Waller factor of neighbor shells) are quantitatively resolved from the EXAFS spectra by comparing the measured EXAFS signal with the model signal. The FEFF models were constructed based on the octahedral $[RhCl_6]^{3-}$ and pseudo-octahedral *cis*-$[RhCl_4(EG)]^-$ complexes, which were expected in the solutions based on ^{103}Rh NMR results.

The rhodium EXAFS spectrum of rhodium in 3.345 $mol\cdot L^{-1}$ LiCl solution can be completely described by the FEFF model based on the structure of the $[RhCl_6]^{3-}$ complex, which comprised one single scattering (SS) path of Rh−Cl and five multiple scattering (MS) paths up to 4.1 Å. The Rh EXAFS spectrum of rhodium in 0.154 $mol\cdot L^{-1}$ LiCl solution can be completely described by the FEFF model based on the structure of the *cis*-$[RhCl_4(EG)]^-$ complex, which comprised four SS paths (Rh−O, Rh−Cl_a, Rh−Cl_b, and Rh−C). Two variable parameters are introduced for each scattering path: coordination shell distance (R) and Debye−Waller factors (σ^2). Coordination numbers (N) are kept fixed at the values of the model complexes. In addition, the amplitude reduction factor ($S_0{}^2$) and the shift of the energy origin of the photoelectron (ΔE_0), common to all scattering paths, are also varied.

To minimize the number of free parameters, some constraints in the EXAFS model of the $[RhCl_6]^{3-}$ complex were implemented in the EXAFS fit by linking the parameters of the Rh−Cl paths with the parameters of the MS paths

(Figure S10).[42] The initial *cis*-$[RhCl_4(\kappa^2\text{-EG})]^-$ conformation used as input for the EXAFS model fit was obtained through DFT optimization (*vide infra*).

2.5. Quantum Chemical Calculations. All quantum chemical calculations were performed using the ORCA 6.0.0 program.[43−48] Geometries were optimized employing the all-electron SARC-ZORA-TZVP basis set for rhodium and the ZORA-def2-TZVP basis set for all other nuclei in combination with the hybrid PBE0 functional.[49−51] This combination and closely matching methods have demonstrated excellent agreement with experimental data for rhodium and other platinum group metals.[49,52,53] The corresponding isotropic absolute shieldings (σ_{iso}) were calculated with the TZVPP variants containing extra polarization functions, which are recommended for NMR calculations.[54] Gauge-including atomic orbitals were employed for the calculation of all shielding tensors. The corresponding chemical shifts were calculated using eq 1. All calculations were caried out using the SARC/J auxiliary basis set, together with the VeryTightOPT and VeryTightSCF convergence criteria.[55] The fine integration grid (DEFGRID3) was employed throughout.

$$\delta_{iso} = 10^6 \times \frac{\sigma_{ref} - \sigma_{sample}}{1 - \sigma_{ref}} \tag{1}$$

To induce the solvation effect on the shifting behavior in NMR spectra, the conductor-like polarizable continuum model (C-PCM), using the van der Waals cavity and the Gaussian Charge Scheme approach, was used.[56−58] Implicit solvation models, like C-PCM, simulate the solvent by placing the solute in a cavity of molecular shape. The interactions of the solute's electric field with the solvent and the solvent's reaction field with the solute are calculated iteratively. In the C-PCM approach, the solvent is treated as an ideal conductor and subsequently corrected by a scaling factor f(ε). For ideal conductors, the electric field generated by the solute is fully canceled in the conductor by the rearrangement of charges. As solvents are not ideal conductors, the scaling factor, based on the relative permittivity, is applied. The exact nature of the scaling factor is model-dependent and is described by eq 2 for the C-PCM model as implemented by ORCA.

$$f(\varepsilon) = \frac{\varepsilon - 1}{\varepsilon} \tag{2}$$

Hence, the electrostatic interaction between the solvent and the solute is solely related to the solvent's permittivity. Unfortunately, implicit solvation models can simulate systems only at infinite dilution. As such, they cannot account for the presence of other species in solution, such as lithium chloride, nor can they accurately model systems with high concentrations of rhodium itself, both of which can significantly influence the system's behavior. More elaborate QM/MM models are crucial for obtaining precise and quantitative results with electrolyte solutions that can accurately treat the formation of double layers around the solute. Such models are beyond the scope of this study and often require extensive sampling and averaging over multiple conformations. Nevertheless, the rather crude C-PCM model has been employed here, as there is no need for exact quantification but rather observation of the overall trends, allowing an initial reasoning for the observed shifting behavior to be extracted. As the model singularly depends on the relative permittivity to determine the extent of electrostatic interaction between the solute and the solvent, the relative permittivity can be arbitrarily increased to model the increased ionic strength and thus increased interaction between the solute and the solvent. This can be justified by considering the effect of salts, such as lithium chloride, in solution on polar solutes. As the ionic strength of solutions increases, the ability of the solution to screen the electrostatic field generated by the solute is increased, while the effective charge of the solute decreases. At very high ionic strengths, the solution will resemble the behavior of conductors, for which the solvent can fully cancel the electric field generated by the solute. Therefore, $\varepsilon = 10000$ was used to represent the high ionic strength solution, modeling conductor-like behavior ($f(\varepsilon) \approx 1$), while $\varepsilon = 38.5505$ was used as the starting point, calculated using the OLI Studio 11.5 software package, representing the relative permittivity of ethylene glycol solution containing 1.25 wt % H_2O.

3. RESULTS AND DISCUSSION

3.1. Identification of Rhodium(III) Complexes through ^{103}Rh NMR Spectroscopy. To investigate the speciation of rhodium(III) in ethylene glycol solution in the absence and presence of LiCl, five compositions (0.0, 0.154, 0.514, 2.541, and 3.346 mol·L^{-1} LiCl), each containing approximately 0.42 mol·L^{-1} Rh, were prepared. By careful control of the NMR settings, it is possible to achieve narrow resonances for ^{103}Rh beyond the secondary isotope effect alone. Although this results in a pattern that can be used as a fingerprint, the splitting pattern might be less clear at first glance, as proper measurements reveal the presence of isotopomer shifts as well. Isotopomers are isomers having the same number of isotopic atoms but differing in their positions.

The origin of the secondary isotope shift in this study can be traced to the presence of chlorido ligands in the complex, giving rise to isotopologues (i.e., species that differ only in their isotopic composition) in solution, each with an abundance determined solely by the natural isotopic ratio of ^{35}Cl (0.755−0.761) and ^{37}Cl (0.245−0.239).[59] The relative abundances can be described using a binomial distribution (eq S2), as each chlorido ligand has an independent probability of being either ^{35}Cl or ^{37}Cl.

Substitution of a lighter isotope (^{35}Cl) with a heavier one (^{37}Cl) reduces vibrational amplitudes, causing increased shielding, a phenomenon known as vibrational shielding.[31,60−62] As a result, the calculated abundances can be ordered with increasing ^{37}Cl content, reflecting the increased shielding in the experimental data. Hence, six theoretical distributions, ranging from $[RhClX]^{2+}$ to $[RhCl_6]^{3-}$, were determined (Figure S11 and Table S3).

All measured NMR spectra are shown in Figure 1. For clarity, NMR patterns are interpreted starting with the 3.346 mol·L^{-1} LiCl solution. This spectrum is dominated by 1 resonance at −262.81 ppm, containing at least 6 individual signals in the envelope. The regularity of the peak positions in the pattern is evident, with an incremental shift of 0.28 ppm (Table S4). This regularity is indicative of the secondary isotope effect, known to be "quasi" additive.[62−64] Visual comparison of the calculated patterns with the experimental data of the 3.346 mol·L^{-1} LiCl solution reveals a clear resemblance to the $[RhCl_6]^{3-}$ distribution. A more precise comparison can be performed by deconvolution of the 6 peaks in the obtained pattern (Figure 2a). Comparison of the relative abundances (integrated surface area) with the theoretical

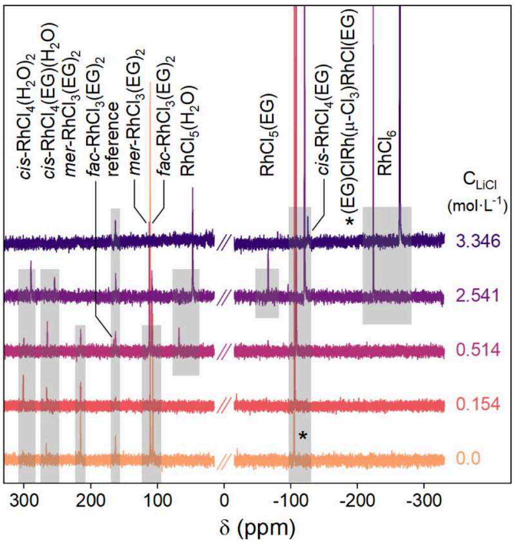

Figure 1. ^{103}Rh NMR spectra of RhCl$_3$·xH$_2$O dissolved in ethylene glycol at varying LiCl concentrations. Gray boxes indicate identified resonances tracked across the LiCl concentrations. Due to the wide spectral width of the NMR spectrum, two separate phase corrections were required.

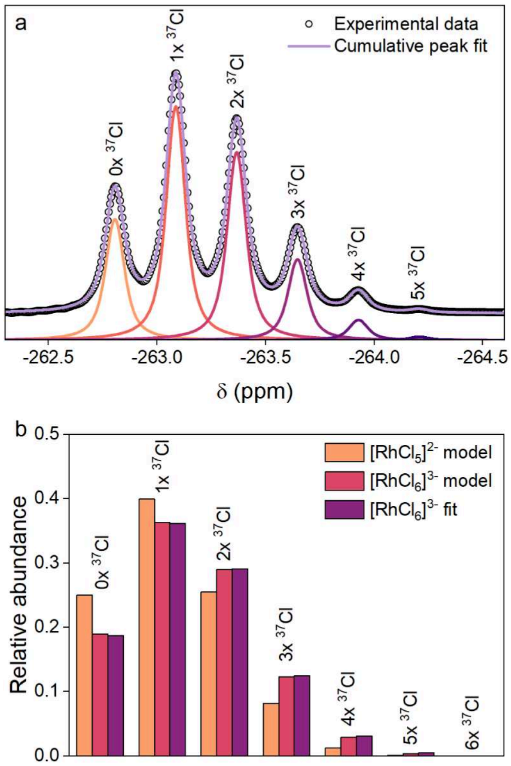

Figure 2. (a) Deconvolution of the ^{103}Rh NMR peak pattern at −262.81 ppm and (b) comparison of the peak areas with the theoretical models for [RhCl$_5$X]$^{2-}$ and [RhCl$_6$]$^{3-}$. Experimental conditions: 3.346 mol·L^{-1} LiCl, LB = 1 Hz.

pattern illustrates the presence of 6 chlorido ligands around the rhodium core, indicating the formation of the octahedral [RhCl$_6$]$^{3-}$ complex at 3.346 mol·L^{-1} (Figure 2b). The most shielded peak, resembling the [Rh^{37}Cl$_6$]$^{3-}$ isotopomer, is not observed in the experimental data. This can be related to its low theoretical abundance (0.02%), so that it cannot be observed in the experimental spectra, regardless of how high the S/N ratio was. An identical peak pattern is observed for rhodium in the 2.541 mol·L^{-1} LiCl solution (Figure S12). Interestingly, the [RhCl$_6$]$^{3-}$ peak position is significantly more deshielded in the 2.541 mol·L^{-1} LiCl solution (−223.07 ppm) compared to the identical peak pattern at 3.346 mol·L^{-1} LiCl (−262.81 ppm). As no isomer exists for [RhCl$_6$]$^{3-}$, the shielding behavior with increased LiCl content can be linked to changes in its environment, discussed in more detail further below in the text.

A second major pattern is observed in 0.154, 0.514, 2.541, and 3.346 mol·L^{-1} LiCl solutions at −105.40, −107.70, −120.23, and −125.20 ppm, respectively. The peak pattern is, however, significantly more complex than the one for [RhCl$_6$]$^{3-}$ and necessitates more insight into the exact stereochemistry of the complex to properly assign the corresponding species. As a start, the relative position in comparison with the [RhCl$_6$]$^{3-}$ pattern can already act as guidance for identifying the correct species.

Explanations of the chemical shift for transition metal NMR usually rely on the total isotropic shielding (σ_{iso}) being separable into a diamagnetic (σ_d) and paramagnetic (σ_p) contribution, caused by the electrons in the ground state and the singlet excited state, respectively. The former is often considered constant, as this term is mostly determined by the core electrons, which are mostly independent of their environment. The shifting behavior is thus often reduced to the paramagnetic contribution. The underlying cause of paramagnetic shielding is typically further split into three factors:[31] (a) the HOMO−LUMO gap (ΔE), (b) the average distance of the valence electrons to the core, and (c) the imbalance of the electrons in the valency orbitals caused by the formation of molecular orbitals. The latter factor, based on the electron distribution in the molecular orbitals, can be ignored as all considered complexes are low-spin, with a $t_{2g}^6 e_g^0$ configuration. The effect of the remaining two parameters can be illustrated by eq 3 derived by Juranić for d^6- complexes starting from the original Ramsey equations, with μ_0 representing the permittivity in vacuum, μ_B the Bohr magneton, $\langle r_d \rangle_F$ the average distance of the d-electrons in a free ion, β the nephelauxetic ratio, and ΔE the HOMO−LUMO gap.[65−69]

$$\sigma_P = -8\frac{\mu_0 \mu_B^2}{\pi} \langle r_d^{-3} \rangle_F \frac{\beta}{\Delta E} \tag{3}$$

Even though the Ramsey equations have been superseded for a long time by newer and more quantitatively accurate methods, the equation derived by Juranić remains a useful and straightforward way to explain the underlying trends for d^6-complexes. With this, it is clear that a decrease in ΔE causes an increase in paramagnetic deshielding, theoretically explained by the increase in state mixing. Conversely, the effect of the average distance of the valency electrons to the core, represented by the $\langle r_d^{-3} \rangle_F \cdot \beta$ term, on paramagnetic deshielding is explained by the decrease in magnetic effects with increasing distance to the core. Therefore, the shifting behavior is often qualitatively explained using the spectrochemical and nephelauxetic series, reflecting the changes in ΔE and cloud expansion, respectively. Although the chlorido ligand is considered a slightly weaker field ligand than the aqua ligand, both ligands are considered weak-field; thus, a limited difference caused by differences in ΔE could be expected. The nephelauxetic effects, however, are distinct for aqua and

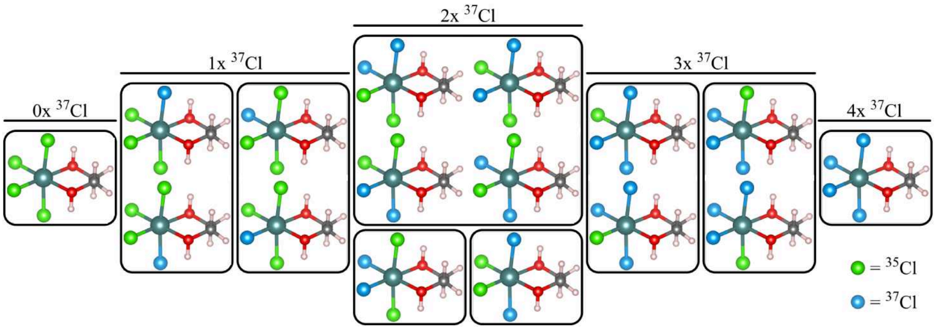

Figure 3. Isotopologues and isotopomers of *cis*-$[RhCl_4(\kappa^2\text{-EG})]^-$. Black boxes indicate that isotopologues should have the same chemical shifts.

chlorido ligands as a result of the particularly strong cloud expansion for halogen atoms. Therefore, ligands such as water and ethylene glycol, which are good σ-donors, poor π-acceptors, and have low polarizability, cause the strongest deshielding.[31] Following this logic, exchanging chlorido ligands with ethylene glycol should cause deshielding. As expected, all main peak patterns are observed at higher shift values compared to the $[RhCl_6]^{3-}$ pattern described earlier, indicating the exchange of chlorido ligands.

With the general trends in mind, the second major peak pattern might be linked to $[RhCl_4X]^-$ or $[RhCl_5X]^{2-}$ type complexes. To establish an initial starting point for deconvolution, all conformations (*cis*/*trans*) and their corresponding isotopologues and isotopomers need to be more thoroughly addressed. Figure 3 illustrates and groups all combinations of isotopomers for each isotopologue of the *cis*-$[RhCl_4(EG)]^-$ complex.

Although both the *cis* and *trans* conformations have the same number of isotopologues, the underlying number of isotopomers for each isotopologue is different and dependent on the stereochemistry. As these different isotopomers have slightly different vibrational properties, the peak position of each isotopomer will slightly deviate from one another. Hence, the corresponding abundances determined by the binomial distribution should be further broken down to each probability of each isotopomer. From Figure 3, it can be derived that the *cis* conformation has an $A^{100} \mid B^{50:50} \mid C^{16.7:66.7:16.7} \mid D^{50:50} \mid E^{100}$ configuration, where the letters denote the isotopologue (A = 0× ^{37}Cl until E = 4× ^{37}Cl) and the superscripts represent the relative abundance (in %) of each isotopomer within each isotopologue. On the contrary, the *trans*-configuration is described by $A^{100} \mid B^{100} \mid C^{33.3:66.7} \mid D^{100} \mid E^{100}$ and thus contains a distinctively different pattern (Figure S13).

Using this, a robust deconvolution without the need for further fitting restrictions can be obtained (Figure 4a). A comparison of the relative abundances of each isotopomer indicates that the pattern is consistent with the *cis*-$[RhCl_4(\kappa^2\text{-EG})]$ conformation (Figure 4b).

Two main peak patterns, more deshielded than the *cis*-$[RhCl_4(\kappa^2\text{-EG})]^-$ pattern, are observed at 111.08 and 107.24 ppm (0 mol·L^{-1} LiCl), both resembling the theoretical trichlorido model. The two plausible configurations, *fac* and *mer*, also observed in aqueous solution,[15] have an $A^{100} \mid B^{100} \mid C^{100} \mid D^{100}$ and $A^{100} \mid B^{66.7:33.3} \mid C^{33.3:66.7} \mid D^{100}$ configuration, respectively, as illustrated in Figure 5. Based on these configurations, the peaks can be assigned, with the peak pattern at 111.08 ppm corresponding to the *mer* conformation (Figure 6a), while the peak pattern at 107.24 ppm corresponds to the *fac* conformation (Figure 6b). Peak deconvolution confirms the complexes to be trichlorido complexes (Figure 6c).

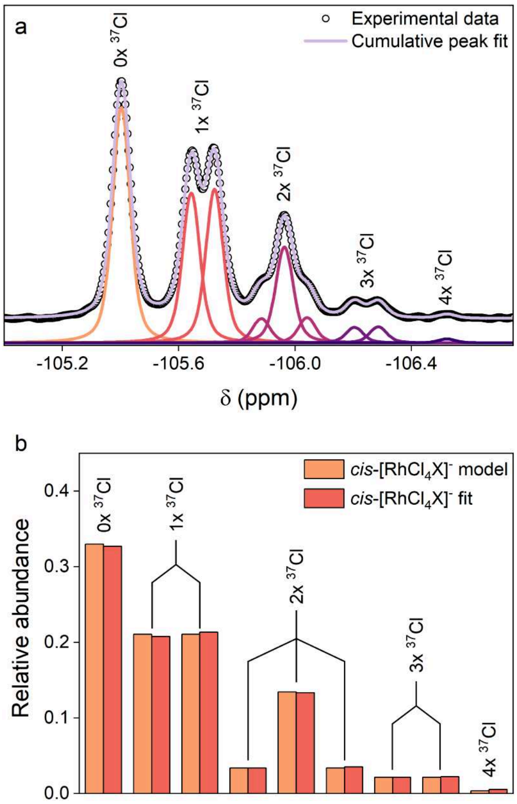

Figure 4. (a) Deconvolution of the ^{103}Rh NMR peak pattern at −105.40 ppm and (b) comparison of the deconvolved peak areas with the theoretical model of a *cis*-$RhCl_4X$ complex. Experimental conditions: 0.154 mol·L^{-1} LiCl, LB = 0.1 Hz.

Due to the lower intensity of the trichlorido complexes compared to $[RhCl_6]^{3-}$ and *cis*-$[RhCl_4(\kappa^2\text{-EG})]^-$, more line broadening was required to enhance the S/N. This processing step can partially or fully obscure the fine structure within the peak patterns, making distinction between closely related species more challenging. Comparison with complementary information, such as their aqueous counterparts, can be essential for accurate assignment. Notably, the peak pattern of the *mer*-isomer exhibits substantially greater broadening than that of the *fac*-isomer. Since both species are expected to experience similar intrinsic broadening and thus similar overlap, the additional broadening observed in the *mer* pattern suggests the presence of additional splitting within the pattern, further supporting its assignment.

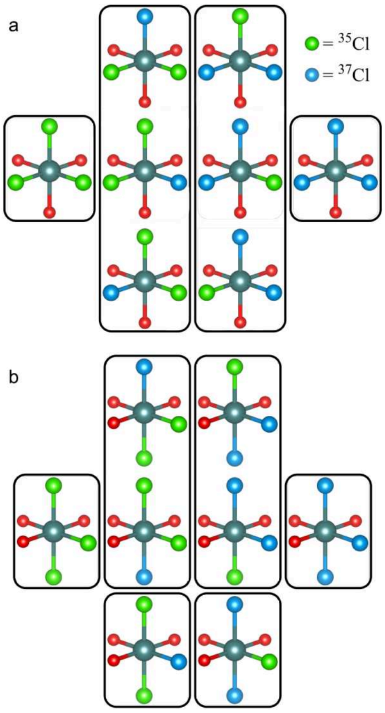

Figure 5. Isotopologues and isotopomers of (a) *fac-* and (b) *mer-*$RhCl_3X$ type complexes. Black boxes indicate isotopologues that should have the same chemical shifts. The *mer*-isomer should have six distinct peaks, whereas the *fac*-isomer should have four distinct peaks.

Although the elucidation method employed in this study is well-suited for the determination of the precise conformation around the rhodium core, the full configuration, containing the coordinated solvent molecules, must be inferred subsequently. Since direct experimental evidence for the conformation of the ethylene glycol beyond the oxygen atom is not available, the choice of the configuration may remain partially speculative, as coordination through both monodentate and bidentate bonding modes is feasible. Nevertheless, the existence of numerous cobalt, nickel, and copper complexes featuring bidentately bonded ethylene glycol ligands,[70−72] alongside a wide variety of examples for nickel, platinum, iridium, and rhodium itself with the structurally similar ethylenediamine ligand,[73−75] strongly supports the capability of ethylene glycol to act as a bidentate ligand. Accordingly, in this study, ethylene glycol is modeled as a bidentate ligand, as its ability to coordinate in this manner is well established and is expected to be energetically favorable compared with its monodentate counterpart.

This favoring in bidentate bonding questions the existence of *fac-* and *mer-*$[RhCl_3(\kappa^2\text{-EG})(\kappa^1\text{-EG})]$ complexes. Nevertheless, the unambiguous assignment of both patterns points to the presence of these trichlorido complexes. Hence, the existence of several ethylene glycol-bridged dirhodium(III) complexes (Figure 7) is hypothesized, similar to what has previously been proposed for indium complexation in ethylene glycol solution.[76] Due to the lack of direct evidence for their existence, both isomers will continue to be referred to as *fac-* and *mer-*$[RhCl_3(\kappa^2\text{-EG})(\kappa^1\text{-EG})]$ rather than their hypothesized ethylene glycol-bridged counterparts.

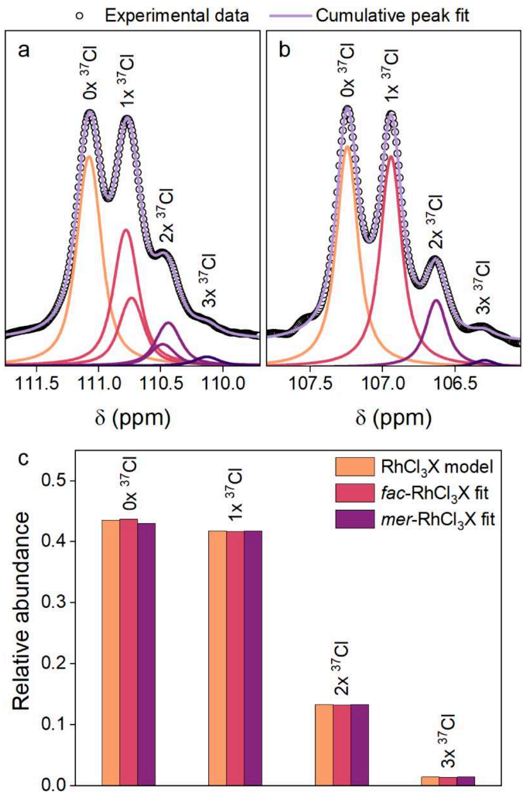

Figure 6. Deconvolution of the ^{103}Rh NMR peak pattern at (a) 111.08 and (b) 107.24 ppm. (c) Comparison of the deconvolved peak areas with the theoretical model of a $RhCl_3X$ complex. Experimental conditions: 0 mol·L^{-1} LiCl, LB = 2 Hz. Fitting constraints: the peak areas within an isotopologue were constrained to achieve reliable fitting results for the *mer*-$RhCl_3X$ pattern.

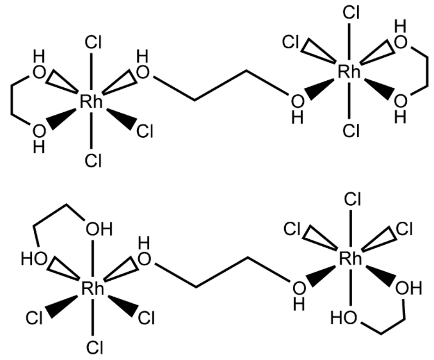

Figure 7. Hypothesized ethylene glycol-bridged dirhodium(III) complexes.

One last distinct peak pattern is observed in the spectrum of the 0 mol·L^{-1} LiCl solution between −104.45 and −105.69 ppm. This pattern is notably different from those previously described. It is more shielded compared with both trichlorido complexes, suggesting the presence of a species with a greater number of chlorido ligands. Interestingly, its position aligns closely with the previously identified *cis*-$[RhCl_4(\kappa^2\text{-EG})]^-$ complex. An initial indication can be obtained by a comparison of the chemical shift as a function of the LiCl concentration (Figure 8). Although the origin of this shifting behavior will be addressed later in more detail, the linear trend, also observed for the other determined patterns, provides a basis for assigning peak patterns in spectra with suboptimal S/N ratios if several spectra at different LiCl concentrations are available. Based on this trend and higher shielding in comparison to the $[RhCl_3(\kappa^2\text{-EG})(\kappa^1\text{-EG})]$ complexes, the pattern would be

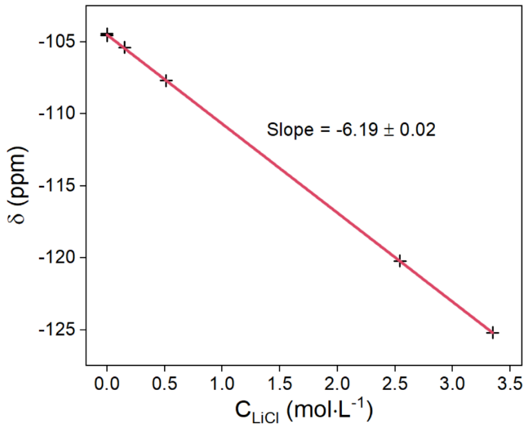

Figure 8. Shifting behavior in the ^{103}Rh NMR spectrum of the *cis*-$RhCl_4(\kappa^2$-EG) complex as a function of the LiCl concentration.

expected to correspond to the *cis*-$[RhCl_4(EG)]^-$ complex. This conclusion presents two challenges: 1) no rhodium complex containing fewer than three chlorido ligands has been identified, and no additional chloride source is introduced into the solution with 0 mol·L^{-1} LiCl, making the formation of a tetrachlorido complex as such impossible; and 2) the observed peak pattern deviates strongly from the characteristic shapes of any described and theoretically expected pattern. The latter is most likely explained by the presence of two or more overlapping peak patterns. The shift between the first two peaks of 0.11 ppm, which is well below the observed and expected shift for secondary isotope effects from chlorido ligands, aligns with this hypothesis. Unfortunately, even with the high resolution obtained for this sample, it is insufficient to fully resolve these overlapping patterns without prior knowledge, and significant restrictions during the deconvolution process would be necessary.

Both the lack of chloride anions and the observed complex pattern can be addressed if a chlorido-bridged dirhodium(III) complex is considered. To the best of our knowledge, no chlorido-bridged dirhodium complexes have been reported in aqueous solutions. However, a $[Cl_3Rh(\mu\text{-}Cl)_3RhCl_3]^{3-}$ species is believed to form upon extraction from aqueous media using quaternary ammonium salts.[12]

Based on the agreement of the peak position with the slope of the *cis*-$[RhCl_4(\kappa^2\text{-EG})]^-$ shift values, a $[(\kappa^2\text{-EG})ClRh(\mu\text{-}Cl)_3RhCl(\kappa^2\text{-EG})]^+$ complex would be expected (Figure 9a). As the secondary isotope effect for chlorido ligands only significantly manifests when direct coordination occurs, the patterns of each rhodium(III) center can be approximated by a *cis*-$[RhCl_4(\kappa^2\text{-EG})]^-$ pattern. Nevertheless, two isomers exist, each of which will exhibit a slightly different resonance frequency, which explains the overlapping patterns.

To fit the complex peak pattern, two theoretical *cis*-$[RhCl_4(\kappa^2\text{-EG})]^-$ patterns were used (Figure 9b). For this, both the peak areas and the peak positions of the overlapping patterns were restricted to a single parameter for the area and position, allowing only an overall shift of the *cis*-$[RhCl_4(\kappa^2\text{-EG})]^-$ patterns while adhering to the theoretically calculated relative ratios. This approximation, which neglects the effect of chlorido bridging on the isotope pattern, closely resembles the experimental data, supporting the initial hypothesis.

3.2. Speciation Study by EXAFS.

Next to ^{103}Rh NMR spectroscopy, EXAFS spectroscopy is particularly useful for the determination and characterization of coordination complexes,

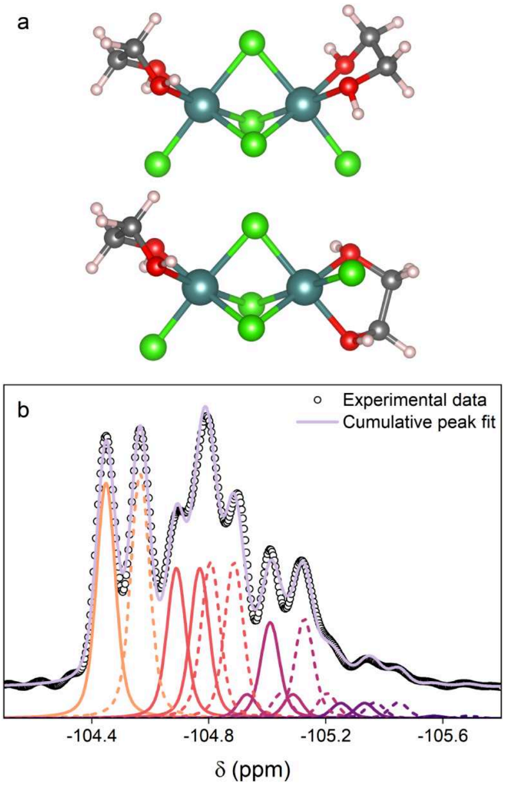

Figure 9. (a) Two possible isotopomers of the $[(\kappa^2\text{-EG})ClRh(\mu\text{-}Cl)_3RhCl(\kappa^2\text{-EG})]^+$ complex and (b) approximated deconvolution of the complex peak pattern in the ^{103}Rh NMR spectrum at −104.45 ppm by fitting two theoretical *cis*-$[RhCl_4(\kappa^2\text{-EG})]^-$ patterns (dashed and nondashed). Conditions: 0 mol·L^{-1} LiCl, LB = 0.1 Hz. Fitting constraints: peak positions and relative peak areas for both patterns were restricted.

which is ideal for verifying the results obtained from ^{103}Rh NMR spectra. Given the hypothesized formation of a $[Cl_3Rh(\mu\text{-}Cl_3)RhCl_3]^{3-}$ complex after extraction from aqueous solution,[12] and the presence of a dirhodium(III) complex in ethylene glycol at 0 mol·L^{-1} LiCl (*vide supra*), the ability to form dirhodium(III) complexes at other LiCl concentrations can be questioned. Secondary isotope shifting patterns are incapable of differentiating between mono- and dirhodium(III) complexes, as the effect is only noticeable for atoms in the direct vicinity of the rhodium core. As a result, the ability to identify dirhodium complexes relies solely on the small shielding differences between their stereoisomers, as illustrated for the proposed $[(\kappa^2\text{-EG})ClRh(\mu\text{-}Cl)_3RhCl(\kappa^2\text{-EG})]^+$ complex (*vide supra*). Since the $[RhCl_6]^{3-}$ and $[Cl_3Rh(\mu\text{-}Cl_3)RhCl_3]^{3-}$ complexes lack stereoisomers, they cannot be distinguished by ^{103}Rh NMR.

To verify the conclusions deduced from ^{103}Rh NMR and to distinguish between $[RhCl_6]^{3-}$ and $[Cl_3Rh(\mu\text{-}Cl_3)RhCl_3]^{3-}$ complexation, EXAFS spectroscopy was employed. Given the distortion of the perfect octahedral structure when bridging occurs, such as in the case of the $[Cl_3Rh(\mu\text{-}Cl_3)RhCl_3]^{3-}$ complex, further validation can be obtained through the fitting of the MS paths. The Rh EXAFS spectrum of the 3.345 mol·L^{-1} LiCl solution can be completely described by the $[RhCl_6]^{3-}$ FEFF model (Figure 10). With this, a single shell of six chlorido ligands at a distance of 2.349(2) Å was obtained (Table 1), confirming the results based on its isotope splitting pattern. The low *R*-factor of 0.0067 for this fitting indicates

https://doi.org/10.1021/acs.inorgchem.5c02591
Inorg. Chem. XXXX, XXX, XXX−XXX

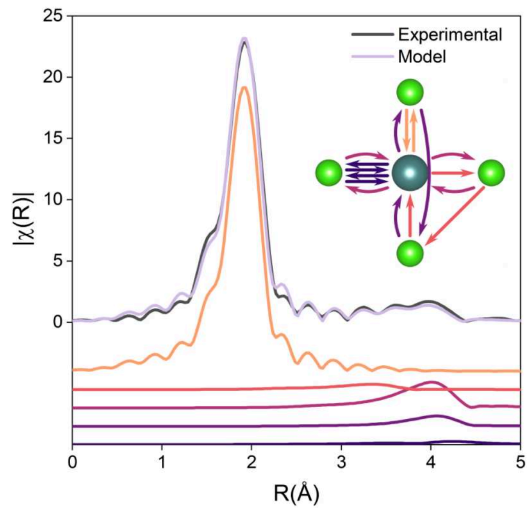

Figure 10. Magnitude of the Fourier-transformed EXAFS spectra of the 3.345 mol·L^{-1} LiCl solution and its fitted FEFF model of a $[RhCl_6]^{3-}$ complex. Fitting constraints: *R*-range = 1.1−4.5.

Table 1. EXAFS Best Fit Parameters of the $[RhCl_6]^{3-}$ Model Using the SS and All MS Paths up to Four Legs[a,b]

Scattering path	S_0^2	*N*	*R* (Å)	σ^2
[Rh] > Cl > [Rh]	0.95(3)	6	2.349(2)	0.0035(2)
Collinear triple scattering [Rh] > Cl_1 > [Rh] > Cl_2 > [Rh]	0.95(3)	6	4.698(4)	0.0070(4)
Collinear double scattering [Rh] > Cl_1 > Cl_2 > [Rh]	0.95(3)	6	4.698(4)	0.0070(4)
Rattle scattering [Rh] > Cl_1 > [Rh] > Cl_1 > [Rh]	0.95(3)	6	4.698(4)	0.0141(8)
Triangular scattering [Rh] > Cl_1 > Cl_3 > [Rh]	0.95(3)	24	4.010(3)	0.0070(4)

[a]Conditions: 3.346 mol·L^{-1} LiCl. [b]*R*-factor = 0.0067.

excellent agreement between the model and the experimental data, providing no evidence for the need for an additional single scattering (SS) path ([Rh] > Rh > [Rh]). The triangular and all collinear paths (double, triple, and rattle scattering paths) were considered as well. With this, the MS paths closely matched the χ(R) data between 3 and 4.5 Å, confirming the undistorted octahedral geometry of the $[RhCl_6]^{3-}$ complex.

The absence of major NMR signals besides the *cis*-$[RhCl_4(\kappa^2\text{-EG})]^-$ pattern in the 0.154 mol·L^{-1} LiCl solution allows validation of this complex with EXAFS spectroscopy as well. Due to the lower symmetry of the complex, an additional single scattering shell is required to model the nonequal bond distances of the chlorido ligands (Figure 11 and Table 2). As with the previous EXAFS model, the excellent agreement between the model and the experimental data (*R*-factor = 0.0059) indicates that all significant scattering contributions are adequately described. Given the absence of significant residuals, no indication of the presence of a [Rh] > Rh > [Rh] SS path was found. Additional validation through fitting of the MS paths is less reliable in this case, as the high number of MS contributions, each strongly dependent on the precise conformation of the complex, prevents a robust fit.

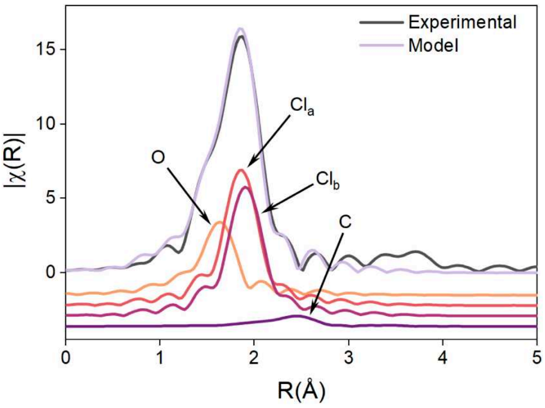

Figure 11. Magnitude of the Fourier-transformed EXAFS spectra of the 0.154 mol·L^{-1} LiCl solution and its fitted FEFF model of a *cis*-$[RhCl_4(\kappa^2\text{-EG})]^-$ complex. Fitting constraints: *R*-range = 1.1−3.

Table 2. EXAFS Best Fit Parameters of Rhodium in 0.154 mol·L^{-1} LiCl Solution[a]

Scattering path	S_0^2	*N*	*R* (Å)	σ^2
[Rh] > O > [Rh]	0.95	2	2.06(2)	0.003(1)
[Rh] > Cl_a > [Rh]	0.95	2	2.294(6)	0.0025(4)
[Rh] > Cl_b > [Rh]	0.95	2	2.341(6)	0.0025(4)
[Rh] > C > [Rh]	0.95	2	2.95(7)	0.007(8)

[a]*R*-factor = 0.0059.

3.3. Rhodium-103 Shifting Behavior. Noticeable changes of the chemical shifts for all determined complexes are observed with increasing LiCl content. As identified before, a remarkable linear trend for the *cis*-$[RhCl_4(\kappa^2\text{-EG})]^-$ chemical shift as a function of the LiCl concentration exists (*vide supra*, Figure 8). Unfortunately, the limited LiCl range in which the other species exist limits the number of determinable points for the identification of similar trends (Figure S14). Regardless, the exact nature of the trend is less of a concern, as it is the substantial difference in both the magnitude and shifting direction that illustrates a potential additional tool for the identification of rhodium species, even with the limited S/N ratios obtained (Table 3). The differences in shifting behavior seem to be primarily influenced by the number of chlorido ligands.

Table 3. Direction of the Chemical Shifts in the ^{103}Rh NMR Spectra and Their Corresponding Slopes as a Function of LiCl Concentration

Complex	NMR shift[a]	Slope (*δ* vs [LiCl])
$[RhCl_6]^{3-}$	Shielding	−49.4
cis-$[RhCl_4(\kappa^2\text{-EG})]^-$	Shielding	−6.2
fac-$[RhCl_3(\kappa^2\text{-EG})(\kappa^1\text{-EG})]$	Deshielding	2.4
mer-$[RhCl_3(\kappa^2\text{-EG})(\kappa^1\text{-EG})]$	Deshielding	2.5

[a]Shifting with increasing LiCl concentration.

To gain deeper insight into the underlying cause of the chemical shifting behavior with an increasing LiCl concentration, quantum mechanical (QM) approaches are crucial. The main complexes ($[RhCl_6]^{3-}$, *cis*-$[RhCl_4(\kappa^2\text{-EG})]^-$, *fac*-$[RhCl_3(\kappa^2\text{-EG})(\kappa^1\text{-EG})]$, and *mer*-$[RhCl_3(\kappa^2\text{-EG})(\kappa^1\text{-EG})]$) were optimized, and the corresponding shieldings were calculated.

The effect of increasing interaction between the solute and solvent for all species shows linear trends between the total

Table 4. Diamagnetic, Paramagnetic, and Total Isotropic Shieldings alongside the HOMO/LUMO Gaps of All the Main Rhodium(III) Complexes

Complex	$f(\varepsilon)$	σ_{dia}	σ_{para}	σ_{tot}	ΔE
$[RhCl_6]^{3-}$	0.9741	4588.792	−13767.358	−9178.565	4.741
	0.9999	4588.880	−13708.313	−9119.434	4.748
cis-$[RhCl_4(\kappa^2\text{-EG})]^-$	0.9741	4594.063	−13118.007	−8523.943	4.822
	0.9999	4594.061	−13116.714	−8522.658	4.831
fac-$[RhCl_3(\kappa^2\text{-EG})(\kappa^1\text{-EG})]$	0.9741	4596.993	−13376.781	−8779.787	4.823
	0.9999	4596.975	−13387.894	−8790.920	4.835
mer-$[RhCl_3(\kappa^2\text{-EG})(\kappa^1\text{-EG})]$	0.9741	4597.057	−13367.750	−8764.165	4.814
	0.9999	4597.020	−13368.475	−8771.455	4.823

isotropic shieldings and the scaling factor (Figure S15), all of which align with the experimental trends identified previously. The implementation of solvation effects through C-PCM appears to cause an underestimation of the shielding effect for the *cis*-$[RhCl_4(\kappa^2\text{-EG})]^-$ complex while slightly overestimating the deshielding effects for both trichlorido complexes. This deviation is anticipated and will most likely result from an overestimation of the interaction between the oxygen atoms of the ethylene glycol ligand and the electrolyte solution. When the scaling factor is arbitrarily increased to model the interaction of anionic chlorido ligands with the electrolyte solution, it inadvertently overestimates the interaction of the neutral ethylene glycol ligand with its surroundings, as no distinct charge double layer forms around ethylene glycol.

3.4. Cause of Chemical Shifts in Rhodium-103 NMR Spectra.

The significant differences in both magnitude and direction of the chemical shifts in the ^{103}Rh NMR spectra raise questions about the origin of this behavior and suggest a more nuanced combination of several phenomena underlying the observed trends. To the best of our knowledge, this behavior has not yet been described, and pinpointing the main factors based on the general ^{103}Rh NMR behavior is not feasible without additional information. To obtain more insight into the origin of these chemical shifts, we evaluated the shielding factors and HOMO/LUMO gaps of each complex (Table 4).

Before we delve into the causes of the observed trends, it is essential to first examine the structural changes of the complexes as a response to the increased interaction with their surroundings. In the absence of coordinating oxygen atoms, all Rh−Cl bonds tend to slightly contract with an increasing scaling factor (Figure 12a). This observation likely arises from the screening effect of the solvent, which reduces the Coulombic repulsion between the negatively charged chlorido ligands and leads to a reduction in the effective charge.

In the presence of a coordinating oxygen atom, a more complex interplay is observed. Although the Coulombic repulsion is still screened between the chlorido ions, it simultaneously reduces the electrostatic attraction between the rhodium(III) center and the chlorido ligands as well. The exact change in geometry is thus dependent on the nature and position of the ligands. When the orbitals of opposing bonds in an octahedral ($[RhCl_6]^{3-}$) or quasi-octahedral (*cis*-$[RhCl_4(\kappa^2\text{-EG})]^-$, *fac*-$[RhCl_3(\kappa^2\text{-EG})(\kappa^1\text{-EG})]$, and *mer*-$[RhCl_3(\kappa^2\text{-EG})(\kappa^1\text{-EG})]$) complexes strongly overlap, they strongly influence each other.

This interplay between several effects is evident in the *fac*-$[RhCl_3(\kappa^2\text{-EG})(\kappa^1\text{-EG})]$ complex (Figure 12c), which highlights that the contraction of the Rh−O bond is energetically more favorable than the contraction of the Rh−Cl bond. The

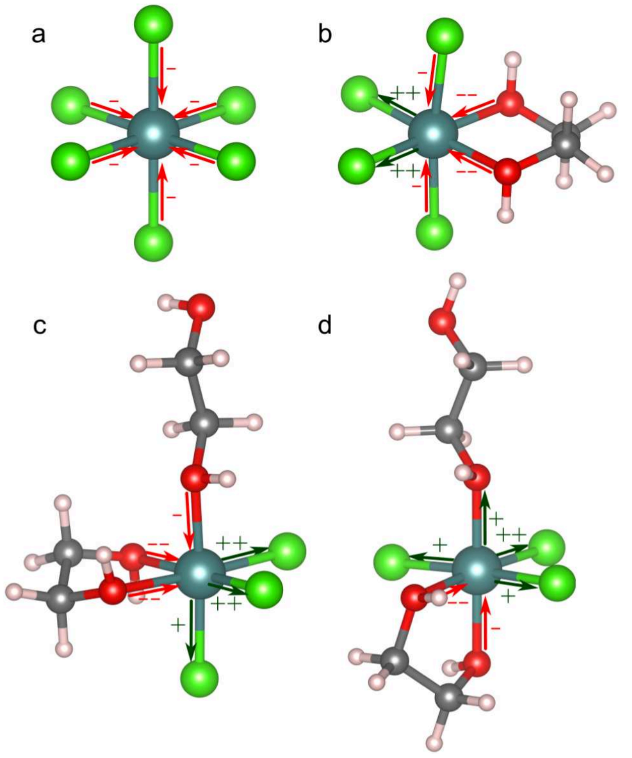

Figure 12. Geometric changes of (a) $[RhCl_6]^{3-}$, (b) *cis*-$[RhCl_4(\kappa^2\text{-EG})]^-$, (c) *mer*-$[RhCl_3(\kappa^2\text{-EG})(\kappa^1\text{-EG})]$, and (d) *fac*-$[RhCl_3(\kappa^2\text{-EG})(\kappa^1\text{-EG})]$ induced by an increased scaling factor.

Rh−O bond lengths associated with a bidentately coordinating ethylene glycol molecule and their corresponding opposing Rh−Cl bonds are notably more affected than those related to the monodentately bonded ones. This observation is most likely related to the higher steric hindrance of the monodentately bonded ethylene glycol ligand, which counteracts the contraction of the Rh−O bond slightly more.

The geometrical changes of the *cis*-$[RhCl_4(\kappa^2\text{-EG})]^-$ complex (Figure 12b) can be explained in an analogous way by the opposing (axial) chlorido bonds contracting, as observed for the $[RhCl_6]^{3-}$ complex, while the equatorial bond changes are similar to the behavior explained for the *fac*-$[RhCl_3(\kappa^2\text{-EG})(\kappa^1\text{-EG})]$ complex. The axially positioned chlorido bonds exhibit a significantly smaller contraction in comparison with that in the $[RhCl_6]^{3-}$ complex, indicating a small but non-negligible effect of the contraction of the Rh−O bonds in the equatorial position.

Finally, the *mer*-$[RhCl_3(\kappa^2\text{-EG})(\kappa^1\text{-EG})]$ complex aligns with the behavior of its *fac* counterpart in the case of the opposing bonds with oxygen and chlorine (Figure 12d).

However, the opposing oxygen bonds seem to compete and strongly reduce their ability to contract, resulting even in a slight elongation of the monodentately bonded ethylene glycol ligand, in agreement with the slightly lower favorability of contracting the monodentate bonds, as described earlier for the *fac*-$[RhCl_3(\kappa^2\text{-EG})(\kappa^1\text{-EG})]$ complex.

It is worth noting that a study by Davis et al. related rhodium chemical shift changes upon isotopic substitution to subtle variations in metal−ligand bond lengths, identifying these bond-length changes as the dominant factor.[77] Although these vibrational isotope effects are conceptually distinct from the solvation-induced structural changes discussed here, they underscore the high sensitivity of ^{103}Rh NMR to minor geometric variations and support the notion that solvation-induced structural changes, such as those described above, are key factors in the observed shielding behavior.

As previously discussed, the diamagnetic shielding (σ_D) for rhodium is often considered to be constant.[31,65] A comparison of the calculated shieldings confirms the minimal effect of the diamagnetic contribution to the total shielding of the rhodium nucleus (Table 4).

With the minimal contribution of diamagnetic shielding to the overall chemical shift established, the more influential paramagnetic shielding is examined. For this, changes in paramagnetic shielding as a result of changes in solvation can be attributed to (1) cloud expansion and (2) transition energy (ΔE) (*vide supra*, eq 3). The calculated ΔE values for all complexes increase with an increase in the scaling factor. Based on this trend, a shielding effect across all complexes with increasing LiCl concentration, consistent with the observed behavior of $[RhCl_6]^{3-}$ and *cis*-$[RhCl_4(\kappa^2\text{-EG})]^-$, is expected. However, it should be noted that this interpretation does not account for potential contributions arising from mixing with lower-lying occupied or higher-lying unoccupied molecular orbitals, which may significantly influence the shielding behavior. On the contrary, the cloud expansion can be inferred from the described geometrical changes upon increasing solvation effects. In the case of $[RhCl_6]^{3-}$, the contraction of Rh−Cl bonds enhances orbital overlap, increasing cloud expansion and causing a reduction in paramagnetic deshielding. The high sensitivity of the chemical shift of the $[RhCl_6]^{3-}$ complex to its environment most likely results from a combined effect of shielding caused by increased cloud expansion and increased ΔE.

While the transition energy increases for all complexes, the less sensitive shielding behavior of the *cis*-$[RhCl_4(\kappa^2\text{-EG})]^-$ complex, as well as the deshielding observed for the *mer*- and *fac*-$[RhCl_3(\kappa^2\text{-EG})(\kappa^1\text{-EG})]$ complexes, can be attributed only to a reduction in cloud expansion (i.e., a smaller nephelauxetic effect). The Rh−Cl bonds are primarily responsible for the cloud expansion of the valence orbitals, as explained by the nephelauxetic series. Hence, their elongation (or reduced contraction) with increasing LiCl concentration causes cloud contraction (or reduced cloud expansion), counteracting the shielding trend caused by the increase in ΔE.

3.5. Minor Rhodium(III) Complexes. The fingerprint method in ^{103}Rh NMR spectroscopy becomes problematic or less reliable for the elucidation of minor species in solution, as these inherently suffer from low S/N ratios, even with extended measurement times. Consequently, structure elucidation based solely on this fingerprint method might be highly susceptible to bias or rendered impossible for deconvolution. Alternative approaches, such as comparison of the shifting trends in response to the LiCl concentration and the chemical shift values with those of known species, might be sufficient to help assign or narrow down feasible complexes.

Three peak patterns, observed at 67.92, 265.31, and 300.73 ppm in the 0.514 mol·L^{-1} LiCl solution, are ideal for elucidation as a result of their sufficient S/N ratios, allowing verification through the pattern itself, albeit by constraining all relative abundancies to the theoretical ratios to enable a robust deconvolution. The first of these, at 67.92 ppm (Figure 13), can be deduced based on five observations: 1) The number of peaks present in the pattern indicates the corresponding complex contains at least three chlorido ligands. 2) The signal of the $Rh^{35}Cl_y{}^{37}Cl_1X$ isotopologue does not appear to be significantly broadened in comparison with the $Rh^{35}Cl_y{}^{37}Cl_0X$ signal. This observation implies the isotopologue to be degenerate, only observed for the *fac*-$[RhCl_3X]$ and *trans*-$[RhCl_4X]^-$ complexes, or to contain a relative ratio of the isotopomers which does not cause major broadening of this isotopologue signal, only found for the $[RhCl_5X]^{2-}$ complex (Figure S16). 3) The most intense signal in the pattern does not correspond to the $Rh^{35}Cl_x{}^{37}Cl_0X$ isotopologue. According to the calculated binomial distribution for the trichlorido complexes (Figure S11) and the inability of the most deshielded peak to split (all ^{35}Cl), the most intense peak must always correspond to the $Rh^{35}Cl_y{}^{37}Cl_0X$ signal, regardless of the line broadening applied. Hence, the *fac*-$[RhCl_3X]$ complex can be excluded. 4) The pattern seems to shift to 47.56 ppm ($\Delta\delta$ = 20.38 ppm) in the presence of a 2.541 mol·L^{-1} LiCl solution, which is significantly larger than the shifts observed for the *cis*-$[RhCl_4(\kappa^2\text{-EG})]$ complex at the same LiCl concentrations ($\Delta\delta$ = 12.52 ppm). This large difference in chemical shift indicates that the pattern most likely corresponds to a $[RhCl_5X]^{2-}$ complex. 5) Deconvolution of the pattern, applying constraints based on the *trans*-$[RhCl_4X]^-$ and $[RhCl_5X]^{2-}$ models, confirms that the pattern corresponds to the latter species (Figures 13 and S17). The figures further reveal the need for careful identification through deconvolution rather than basing the result on the overall structure of the splitting pattern alone, as the *trans*-$[RhCl_4X]^-$ pattern resembles these data surprisingly well if the underlying ratios are not taken into account. Further elucidation of the $[RhCl_5X]^{2-}$ complex, which can still be either $[RhCl_5(\kappa^1\text{-EG})]^{2-}$ or $[RhCl_5(H_2O)]^{2-}$, can be achieved by employing its

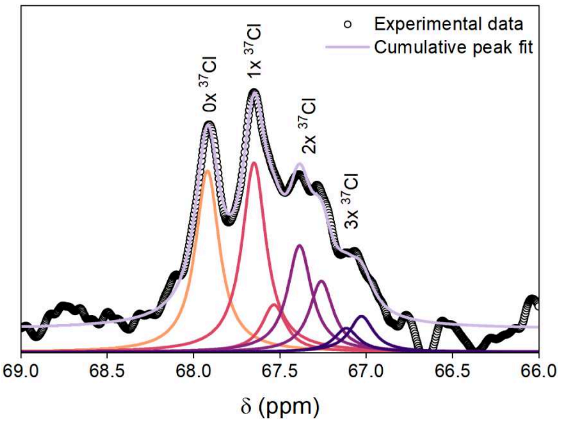

Figure 13. Deconvolution of the ^{103}Rh NMR peak pattern at 67.92 ppm using constraints based on the $[RhCl_5X]^-$ theoretical ratios. Experimental conditions: 0.514 mol·L^{-1} LiCl, LB = 2 Hz.

chemical shift. The chemical shift of 67.92 ppm for the $[RhCl_5X]^{2-}$ complex (0.514 mol·L^{-1} LiCl) does not align with the overall trend of the main complexes, as it is more deshielded than the *cis*-$[RhCl_4(\kappa^2\text{-EG})]^-$ complex at −107.70 ppm. This indicates that the pattern most likely corresponds to the $[RhCl_5(H_2O)]^{2-}$ complex. This conclusion is further supported by the chemical shift of the reference sample (Figure 14; *cis*-$RhCl_4(H_2O)_2]^-$; δ = 163.05 ppm), which reveals a stronger deshielding effect by water compared to ethylene glycol and for which the position of the $[RhCl_5(H_2O)]^{2-}$ complex does align with the generally accepted shielding trend with an increasing number of chlorido ligands. An additional peak pattern, observed at −65.64 ppm (2.541 mol·L^{-1} LiCl), can be assigned identically (Figure S18). Given its more deshielded position relative to the $[RhCl_5(H_2O)]^{2-}$ complex, the pattern is assigned to the $[RhCl_5(\kappa^1\text{-EG})]^{2-}$ species. However, due to its substantially lower intensity, the fitting is less reliable. Moreover, this assignment does not align with the main observed shielding trend, which might be related to the absence of bidentate bonding, which affects the overall chemical shift.

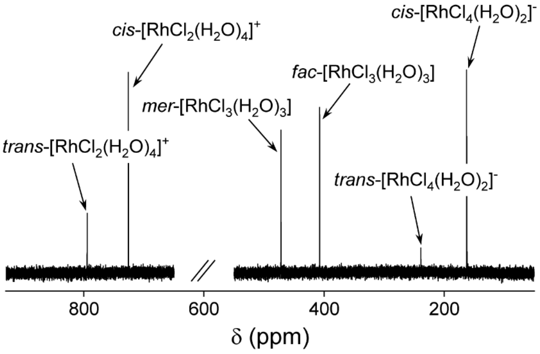

Figure 14. ^{103}Rh NMR spectrum of the aqueous calibration sample used in this study (19 MHz, D_2O). Experimental conditions: 0.433 mol·L^{-1} Rh dissolved in D_2O. Due to the wide spectral width of the NMR spectrum, two separate phase corrections were required.

The second and third peak patterns, observed at 265.31 and 300.73 ppm, respectively, exhibit remarkable similarity, allowing both to be elucidated using the same reasoning: 1) The signal of the $Rh^{35}Cl_y{}^{37}Cl_1X$ isotopologue seems to be nondegenerate, as identified through the significant broadening of the corresponding signal, which is characteristic of complexes of the *mer*-$[RhCl_3X]$, *cis*-$[RhCl_4X]^-$, and $[RhCl_5X]^{2-}$ types, of which the $[RhCl_5X]^{2-}$ type can be excluded as the isotopomer ratio of this isotopologue causes little broadening. 2) The most intense signal in the pattern does not correspond to the $Rh^{35}Cl_x{}^{37}Cl_0X$ isotopologue. This observation rules out any trichlorido complexes as explained before. 3) The NMR signal is shifted to lower chemical shifts with increasing LiCl concentration (Figure S19), reinforcing the conclusion made in point 2. The corresponding slopes as a function of the LiCl concentration, −4.91 ± 0.24 and −4.75 ± 0.29, closely match the one found for the *cis*-$[RhCl_4(\kappa^{2}\text{-EG})]^-$ complex, suggesting the complexes are of the *cis*-$[RhCl_4X]^-$ type. 4) Deconvolution of the pattern, applying constraints based on the *cis*-$[RhCl_4X]^-$ complex, aligns well with the experimental data (Figures 15 and S20a), while the *trans* variant fails to accurately model the two most deshielded isotopologue signals (Figures S20b and S21). The chemical shift values reveal strong deshielding in comparison with the main *cis*-$[RhCl_4(\kappa^2\text{-EG})]^-$ complex, indicating the presence of aqua ligands. Therefore, the signals most likely correspond to *cis*-$[RhCl_4(H_2O)_2]^-$ and *cis*-$[RhCl_4(\kappa^1\text{-EG})(H_2O)]^-$ complexes. Notably, the *cis*-$[RhCl_4(\kappa^1\text{-EG})(H_2O)]^-$ pattern is more deshielded than the corresponding $[RhCl_3(\kappa^2\text{-EG})(H_2O)]$ complexes (*vide infra*), deviating from the generally accepted trends but mirroring the deviation observed for the $[RhCl_5(\kappa^1\text{-EG})]^{2-}$ complex, which also contains an ethylene glycol ligand that can only bind monodentately.

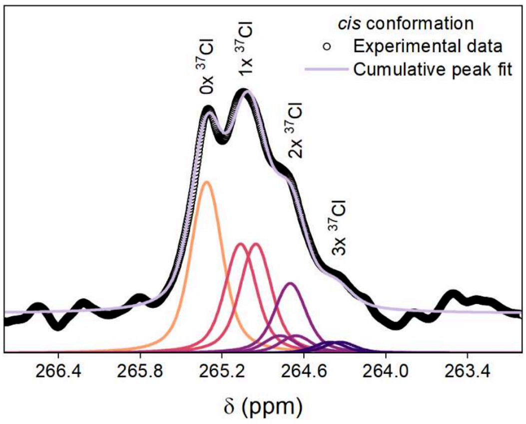

Figure 15. Deconvolution of the ^{103}Rh NMR peak pattern at 265.31 ppm using constraints based on the *cis*-$[RhCl_4X]^-$ theoretical ratios. Experimental conditions: 0.514 mol·L^{-1} LiCl and LB = 3 Hz.

Two further peak patterns observed at 165.65 and 215.12 ppm (0.514 mol·L^{-1} LiCl) are assumed to be linked to the *fac*- and *mer*-$[RhCl_3(\kappa^2\text{-EG})(H_2O)]$ complexes, respectively. Although the assignment is still somewhat speculative, several aspects support this conclusion: 1) Both NMR signals disappear in the 2.514 mol·L^{-1} LiCl solution, suggesting the signals correspond to trichlorido complexes, as only those complexes exhibit the same behavior. 2) The chemical shifts of both complexes are highly deshielded, indicating the presence of water, but do not surpass the chemical shift of the most deshielded *cis*-$[RhCl_4(H_2O)_2]^-$ pattern. 3) The signal at 165.65 ppm (0.514 mol·L^{-1}) exhibits deshielding consistent with the main trichlorido complexes. However, reliable determination of the slope is hindered by a low S/N ratio in the 0 and 0.154 mol·L^{-1} LiCl solutions, further complicated by overlap with the reference signal. 4) The *mer* conformation exhibits stronger deshielding than its *fac* counterpart, as illustrated by the *fac- and mer*-$[RhCl_3(\kappa^2\text{-EG})(\kappa^1\text{-EG})]$ complexes in this study, the *fac- and mer*-$[RhCl_3(H_2O)_3]$ complexes in aqueous solution as proven by Geswindt et al., and the *fac* and *mer* configurations in the calibration spectra (Figure 14).[15] The chemical shift difference between the *fac*- and *mer*-isomers is substantially larger than that observed for the previously characterized trichlorido complexes and more closely resembles the major shift difference for the corresponding complexes in aqueous solution, corroborating the coordination with water. Based on the generally accepted increased shielding with an increased number of chlorido ligands, the tendency of ethylene glycol to favor bidentate bonding, and the arguments presented above, the *mer*- and *fac*-$[RhCl_3(\kappa^2\text{-EG})(H_2O)]$ complexes are proposed. The assignment is, however, still speculative, and a few important sidenotes must be made: 1) The shifting behavior of the pattern at 215.12 ppm deviates from its expected trend in comparison with the other trichlorido complexes, as it does not contain any notable shift within the error margin of calibration of the ^{103}Rh spectra ($\Delta\delta$ = 0.26 ppm). 2) The pattern at 215.12 ppm seems particularly noisy in comparison with signals of similar intensity, which might indicate a more complex species or the presence of kinetic effects.

4. CONCLUSIONS

This study contributed to a better understanding of the coordination chemistry of rhodium in nonaqueous solvents. The main objective was to identify the major rhodium(III) complexes that are formed when rhodium(III) chloride hydrate $RhCl_3 \cdot xH_2O$ is dissolved in ethylene glycol solution and to characterize the corresponding ^{103}Rh NMR spectra, both in the presence and absence of added lithium chloride. Five major rhodium(III) chlorido complexes were identified based on the chemical shift values and isotopologue and isotopomer patterns in the ^{103}Rh NMR spectra: $[RhCl_6]^{3-}$, *cis*-$[RhCl_4(\kappa^2\text{-EG})]^-$, *fac*-$[RhCl_3(\kappa^2\text{-EG})(\kappa^1\text{-EG})]$, *mer*-$[RhCl_3(\kappa^2\text{-EG})(\kappa^1\text{-EG})]$, and $[(\kappa^2\text{-EG})ClRh(\mu\text{-Cl})_3RhCl(\kappa^2\text{-EG})]^+$. The existence of the $[RhCl_6]^{3-}$ and *cis*-$[RhCl_4(\kappa^2\text{-EG})]^-$ complexes was validated by EXAFS spectroscopy. The excellent agreement between the model and the EXAFS data refutes the existence of chlorido-bridged dirhodium(III) complexes in the presence of LiCl.

A remarkable linear trend of the chemical shift as a function of LiCl concentration was observed. Both the magnitude and the direction of the chemical shift as a function of LiCl concentration are characteristics that are useful for distinguishing and identifying the different rhodium(III) complexes. The underlying causes of the shielding/deshielding trends were further elucidated by DFT calculations. A correlation between the shielding/deshielding trends and structural changes in the rhodium(III) complex in response to increased screening of the charges was identified. The corresponding effect of the structural changes on the diamagnetic and paramagnetic shielding could be linked to changes in the HOMO/LUMO gap and cloud expansion (nephelauxetic effect).

The isotopologue/isotopomer patterns, in combination with the shifting characteristics, were used to identify the minor rhodium(III) species despite their noisy ^{103}Rh NMR spectra. The presence of minor amounts of $[RhCl_5(H_2O)]^{2-}$, $[RhCl_5(\kappa^1\text{EG})]^{2-}$, *cis*-$[RhCl_4(H_2O)_2]^-$, *cis*-$[RhCl_4(EG)(H_2O)]^-$, *mer*-$[RhCl_3(\kappa^2\text{-EG})(H_2O)]$, and *fac*-$[RhCl_3(\kappa^2\text{-EG})(H_2O)]$ complexes was proposed.

Although the quantum chemical approach used in this study was able to reproduce the shifting characteristics of the main rhodium(III) complexes and explain the cause of the major differences observed, the use of more elaborate QM/MM approaches is required for the unambiguous identification of the minor species proposed as a hypothesis. Furthermore, while this study contributes to the understanding of rhodium(III) speciation in ethylene glycol solutions, the known sluggish ligand exchange kinetics merit further investigation, since this is particularly important for purification processes based on nonaqueous solvent extraction.

■ ASSOCIATED CONTENT

Supporting Information

The Supporting Information is available free of charge at https://pubs.acs.org/doi/10.1021/acs.inorgchem.5c02591.

^{103}Rh NMR spectra using the alternative (Ξ = 3.16) scale and additional supporting data referenced in this study (PDF)

■ AUTHOR INFORMATION

Corresponding Author

Koen Binnemans − *KU Leuven, Department of Chemistry, Leuven B-3001, Belgium;* orcid.org/0000-0003-4768-3606; Email: Koen.Binnemans@kuleuven.be

Authors

Vincent Cool − *KU Leuven, Department of Chemistry, Leuven B-3001, Belgium;* orcid.org/0000-0002-5249-5012

Gert Steurs − *KU Leuven, Department of Chemistry, Leuven B-3001, Belgium;* orcid.org/0000-0002-9779-7743

Iztok Arčon − *University of Nova Gorica, Laboratory of Quantum Optics, Nova Gorica SI-5000, Slovenia; Jozef Stefan Institute, Department of Low and Medium Energy Physics, Lublijana SI-1001, Slovenia;* orcid.org/0000-0003-4333-4054

Sofía Riaño − *KU Leuven, Department of Chemistry, Leuven B-3001, Belgium;* orcid.org/0000-0002-1049-6156

Tom Van Gerven − *KU Leuven, Department of Chemical Engineering, Leuven B-3001, Belgium;* orcid.org/0000-0003-2051-5696

Complete contact information is available at:
https://pubs.acs.org/10.1021/acs.inorgchem.5c02591

Notes

The authors declare no competing financial interest.

■ ACKNOWLEDGMENTS

The authors would like to thank Johnson Matthey plc for the generous loan of the $RhCl_3 \cdot xH_2O$ salt used in this research through the Johnson Matthey Platinum Group Metal Award Scheme. The authors also thank the Research Foundation-Flanders (FWO Flanders) for the financial support through research grant G0D7421N and infrastructure grant I002720N. This research was further supported by the Slovenian Research and Innovation Agency (Research Core Funding No. P1-0112). We acknowledge DESY (Hamburg, Germany), a member of the Helmholtz Association HGF, for the provision of experimental facilities at the P65 beamline of PETRA III (proposal I-20230851 EC). We would like to thank the P65 beamline staff members Edmund Welter, Sergiu Levcenco, and Tinku Dan for their support during the XAFS experiment. Jakob Bussé is gratefully acknowledged for the design and 3D printing of the measurement cells used for the XAFS experiments.

■ REFERENCES

(1) Medici, S.; Peana, M.; Pelucelli, A.; Zoroddu, M. A. R. (I) Complexes in Catalysis: A Five-Year Trend. *Molecules* **2021**, *26* (9), 2553.

(2) Omrani, M.; Goriaux, M.; Liu, Y.; Martinet, S.; Jean-Soro, L.; Ruban, V. Platinum Group Elements Study in Automobile Catalysts and Exhaust Gas Samples. *Environ. Pollut.* **2020**, *257*, 113477.

(3) Sinisalo, P.; Lundström, M. Refining Approaches in the Platinum Group Metal Processing Value Chain - A Review. *Metals* **2018**, *8* (4), 203.

(4) Hughes, A. E.; Haque, N.; Northey, S. A.; Giddey, S. Platinum Group Metals: A Review of Resources, Production and Usage with a Focus on Catalysts. *Resources* **2021**, *10* (9), 93.

(5) Parker, R. L. *Composition of the Earth's Crust* 6th ed., U.S. Department of the Interior; WA, 1967, *440*.

(6) Fortier, S. M.; Nassar, N. T.; Graham, G. E.; Hammarstrom, J. M.; Day, W. C.; Mauk, J. L.; Seal, R. R. USGS Critical Minerals Review (Annual Review 2021: Critical Minerals). *Min. Eng.* **2022**, *74* (5), 34−48.

(7) Brown, S.; Cole, L.; Cowley, A.; Dickson, J.; Fujita, M.; Girardot, N.; Grant, S.; Jiang, J.; Raithatha, R.; Ryan, M.; et al. *PGM Market Report*; Johnson Matthey, 2024

(8) Zientek, M. L.; Loferski, P. J.; Parks, H. L.; Schulte, R. F.; Seal, R. R., II *Platinum-Group Elements*, Schulz, K. J.; DeYoung, Jr; Seal, R. R., II; Bradley, D. C., Eds.; Professional Paper: Reston, VA, 2017, *1*.

(9) Wolsey, W. C.; Reynolds, C. A.; Kleinberg, J. Complexes in the Rhodium(III)-Chloride System in Acid Solution. *Inorg. Chem.* **1963**, *2* (3), 463−468.

(10) Shlenskaya, V. I.; Efremenko, O. A.; Oleinikova, S. V.; Alimarin, I. P. Chloride Complexes of Rhodium(III) in Aqueous Solutions. *Bull. Acad. Sci. USSR, Div. Chem. Sci.* **1969**, *18* (8), 1525−1527.

(11) Caminiti, R.; Atzei, D.; Cucca, P.; Squintu, F. Coordination of Rhodium(III) in Dilute Aqueous Solutions in Presence of Chloride Anion. *Z. Naturforsch. - Sect. A J. Phys. Sci* **1985**, *40* (12), 1319−1328.

(12) Benguerel, E.; Demopoulos, G. P.; Harris, G. B. Speciation and Separation of Rhodium(III) from Chloride Solutions: A Critical Review. *Hydrometallurgy* **1996**, *40* (1−2), 135−152.

(13) Spiccia, L.; Aramini, J. M.; Crimp, S. J.; Drljaca, A.; Lawrenz, E. T.; Tedesco, V.; Vogel, H. J. Hydrolytic Polymerization of Rhodium(III). Characterization of Various Forms of a Trinuclear Aqua Ion. *J. Chem. Soc. Dalt. Trans.* **1997**, No. 23, 4603−4609.

(14) Svecova, L.; Papaïconomou, N.; Billard, I. Rh(III) Aqueous Speciation with Chloride as a Driver for Its Extraction by Phosphonium Based Ionic Liquids. *Molecules* **2019**, *24* (7), 1391.

(15) Geswindt, T. E.; Gerber, W. J.; Brand, D. J.; Koch, K. R. ^{35}Cl/^{37}Cl Isotope Effects in ^{103}Rh NMR of $[RhCl_n(H_2O)_{6\text{-}n}]^{3\text{-}n}$ Complex Anions in Hydrochloric Acid Solution as a Unique "NMR Finger-Print" for Unambiguous Speciation. *Anal. Chim. Acta* **2012**, *730*, 93−98.

(16) Binnemans, K.; Jones, P. T. Solvometallurgy: An Emerging Branch of Extractive Metallurgy. *J. Sustain. Metall.* **2017**, *3* (3), 570−600.

(17) Cool, V.; Riaño, S.; Van Gerven, T.; Binnemans, K. Separation of Cobalt and Nickel from Ethylene Glycol and Glycerol Feed Solution in Chloride Media by Non-Aqueous Solvent Extraction with Cyphos IL 101. *Sep. Purif. Technol.* **2024**, *333*, 125787.

(18) Li, Z.; Dewulf, B.; Binnemans, K. Nonaqueous Solvent Extraction for Enhanced Metal Separations: Concept, Systems, and Mechanisms. *Ind. Eng. Chem. Res.* **2021**, *60* (48), 17285−17302.

(19) Dewulf, B.; Batchu, N. K.; Binnemans, K. Enhanced Separation of Neodymium and Dysprosium by Nonaqueous Solvent Extraction from a Polyethylene Glycol 200 Phase Using the Neutral Extractant Cyanex 923. *ACS Sustainable Chem. Eng.* **2020**, *8* (51), 19032−19039.

(20) Nguyen, V. T.; Riaño, S.; Aktan, E.; Deferm, C.; Fransaer, J.; Binnemans, K. Solvometallurgical Recovery of Platinum Group Metals from Spent Automotive Catalysts. *ACS Sustainable Chem. Eng.* **2021**, *9* (1), 337−350.

(21) Mann, B. E.; Spencer, C. The Identification of All Ten $[Rh(OH_2)_{6-n}Cl_n]^{3-n}$ Isomers by ^{103}Rh NMR Spectroscopy. *Inorg. Chim. Acta* **1982**, *65*, L57−L58.

(22) Fedotov, M. A.; Belyaev, A. V. O-17 and Rh-103 NMR of Rodium(III) Chloroaquo Complexes. *Koord. Khim.* **1984**, *10* (9), 1236−1242.

(23) Carr, C.; Glaser, J.; Sandström, M. ^{103}Rh NMR Chemical Shifts of All Ten $[RhCl_n(OH_2)_{6-n}]^{3-n}$ Complexes in Aqueous Solution. *Inorg. Chim. Acta* **1987**, *131* (2), 153−156.

(24) Gill, D. S.; Gansow, O. A.; Bennis, F.; Ott, K. C. The Direct Observation of ^{103}Rh NMR. *J. Magn. Reson.* **1979**, *35* (3), 459−461.

(25) Harbor-Collins, H.; Sabba, M.; Leutzsch, M.; Levitt, M. H. ^{1}H-Enhanced ^{103}Rh NMR Spectroscopy and Relaxometry of ^{103}Rh-$(Acac)_3$ in Solution. *Magn. Reson.* **2024**, *5* (2), 121−129.

(26) Carlton, L. Rhodium-103 NMR of Carboxylate and Thiolate Complexes by Indirect Detection Using Phosphorus. *Magn. Reson. Chem.* **1997**, *35* (3), 153−158.

(27) Elsevier, C. J.; Ernsting, J. M.; de Lange, W. G. J. Easy Access to ^{103}Rh N.M.R. Parameters of Rhodium(Organo) Phosphine Compounds via ^{31}P Detected Indirect Two-Dimensional ^{31}P, ^{103}Rh{^{1}H} N.M.R. Spectroscopy. *J. Chem. Soc., Chem. Commun.* **1989**, No. 9, 585.

(28) Agh-Atabay, N. M.; Bayat, C.; Yazgic, U. Spin-Tickling Technique for the Indirect Measurements of the Rh-103 NMR Parameters of Organo-Rhodium Compounds. *Rev. Inorg. Chem.* **1998**, *18* (3), 223−238.

(29) Brevard, C.; Van Stein, G. C.; Van Koten, G. Silver-109 and Rhodium-103 NMR Spectroscopy with Proton Polarization Transfer. *J. Am. Chem. Soc.* **1981**, *103* (22), 6746−6748.

(30) Harris, R. K.; Becker, E. D.; Cabral de Menezes, S. M.; Goodfellow, R.; Granger, P. NMR Nomenclature. Nuclear Spin Properties and Conventions for Chemical Shifts (IUPAC Recommendations 2001). *Pure Appl. Chem.* **2001**, *73* (11), 1795−1818.

(31) Carlton, L. Rhodium-103 NMR. *Annu. Rep. NMR Spectrosc.* **2008**, *63*, 49−178.

(32) Marek, R. NMR Applications, ^{15}N. In *Encyclopedia of Spectroscopy and Spectrometry*; Elsevier, 2017, pp. 110−116. .

(33) Kidd, R. G.; Goodfellow, R. J. Rhodium103Rh. In *NMR and the periodic table*. Harris, R. K.; Mann, B. E. Eds.; Academic Press, 1978. pp. 244−249.

(34) Harris, R. K.; Becker, E. D.; De Menezes, S. M. C.; Granger, P.; Hoffman, R. E.; Zilm, K. W. Further Conventions for NMR Shielding and Chemical Shifts (IUPAC Recommendations 2008). *Magn. Reson. Chem.* **2008**, *46* (6), 582−598.

(35) Petrakis, L. Spectral Line Shapes: Gaussian and Lorentzian Functions in Magnetic Resonance. *J. Chem. Educ.* **1967**, *44* (8), 432.

(36) Keeler, J. *Understanding NMR Spectroscopy*, 2nd ed.; Wiley, 2012.

(37) Higinbotham, J.; Marshall, I. NMR Lineshapes and Lineshape Fitting Procedures. *Annu. Rep. NMR Spectrosc.* **2001**, *43*, 59−120.

(38) Welter, E.; Chernikov, R.; Herrmann, M.; Nemausat, R. A Beamline for Bulk Sample X-Ray Absorption Spectroscopy at the High Brilliance Storage Ring PETRA III. *AIP Conf. Proc.* **2019**, *2054*, 040002.

(39) Newville, M. Larch An Analysis Package for XAFS and Related Spectroscopies. *J. Phys.: Conf. Ser.* **2013**, *430* (1), 012007.

(40) Kas, J. J.; Vila, F. D.; Rehr, J. J. The FEFF Code. In *International Tables for Crystallography*; John Wiley & Sons, Ltd, 2020, pp. 764−769. .

(41) Newville, M. EXAFS Analysis Using *FEFF* and *FEFFIT*. *J. Synchrotron Radiat.* **2001**, *8* (2), 96−100.

(42) Ravel, B. Quantitative EXAFS Analysis. In *X-Ray Absorption and X-Ray Emission Spectroscopy: Theory and Applications*, Van Bokhoven, J. A.; Lamberti, C. Eds.; Wiley, 2016, pp. 281−302

(43) Neese, F.; Wennmohs, F.; Becker, U.; Riplinger, C. The ORCA Quantum Chemistry Program Package. *J. Chem. Phys.* **2020**, *152* (22), 224108.

(44) Neese, F. Software Update: The ORCA Program System—Version 5.0. *Wiley Interdiscip. Rev.: comput. Mol. Sci.* **2022**, *12* (5), 1−15.

(45) Neese, F. An Improvement of the Resolution of the Identity Approximation for the Formation of the Coulomb Matrix. *J. Comput. Chem.* **2003**, *24* (14), 1740−1747.

(46) Neese, F.; Wennmohs, F.; Hansen, A.; Becker, U. Efficient Approximate and Parallel Hartree−Fock and Hybrid DFT Calculations. A 'Chain-of-Spheres' Algorithm for the Hartree−Fock Exchange. *Chem. Phys.* **2009**, *356* (1−3), 98−109.

(47) Helmich-Paris, B.; de Souza, B.; Neese, F.; Izsák, R. An Improved Chain of Spheres for Exchange Algorithm. *J. Chem. Phys.* **2021**, *155* (10), 104109.

(48) Neese, F. The SHARK Integral Generation and Digestion System. *J. Comput. Chem.* **2023**, *44* (3), 381−396.

(49) Rolfes, J. D.; Neese, F.; Pantazis, D. A. All-Electron Scalar Relativistic Basis Sets for the Elements Rb−Xe. *J. Comput. Chem.* **2020**, *41* (20), 1842−1849.

(50) Canal Neto, A.; Ferreira, I. B.; Jorge, F. E.; de Oliveira, A. Z. All-Electron Triple Zeta Basis Sets for ZORA Calculations: Application in Studies of Atoms and Molecules. *Chem. Phys. Lett.* **2021**, *771* (March), 138548.

(51) Lenthe, E. V. *The ZORA Equation*; Vrije Universiteit Amsterdam: Amsterdam, 1996

(52) Debefve, L. M.; Pollock, C. J. Systematic Assessment of DFT Methods for Geometry Optimization of Mononuclear Platinum-Containing Complexes. *Phys. Chem. Chem. Phys.* **2021**, *23* (43), 24780−24788.

(53) Orian, L.; Bisello, A.; Santi, S.; Ceccon, A.; Saielli, G. ^{103}Rh NMR Chemical Shifts in Organometallic Complexes: A Combined Experimental and Density Functional Study. *Chem. - A Eur. J.* **2004**, *10* (16), 4029−4040.

(54) Neese, F. *ORCA Manual Release 6.0.0*; Max-Planck-Institut für Kohlenforschung, 2024.

(55) Weigend, F. Accurate Coulomb-Fitting Basis Sets for H to Rn. *Phys. Chem. Chem. Phys.* **2006**, *8* (9), 1057.

(56) York, D. M.; Karplus, M. A Smooth Solvation Potential Based on the Conductor-Like Screening Model. *J. Phys. Chem. A* **1999**, *103* (50), 11060−11079.

(57) Barone, V.; Cossi, M. Quantum Calculation of Molecular Energies and Energy Gradients in Solution by a Conductor Solvent Model. *J. Phys. Chem. A* **1998**, *102* (11), 1995−2001.

(58) Garcia-Ratés, M.; Neese, F. Effect of the Solute Cavity on the Solvation Energy and Its Derivatives within the Framework of the Gaussian Charge Scheme. *J. Comput. Chem.* **2020**, *41* (9), 922−939.

(59) Meija, J.; Coplen, T. B.; Berglund, M.; Brand, W. A.; De Bièvre, P.; Gröning, M.; Holden, N. E.; Irrgeher, J.; Loss, R. D.; Walczyk, T.; Prohaska, T. Isotopic Compositions of the Elements 2013 (IUPAC Technical Report). *Pure Appl. Chem.* **2016**, *88* (3), 293−306.

(60) Jameson, C. J.; Osten, H. J. Theoretical AspectsTheoretical Aspects of Isotope Effects on Nuclear Shielding. *Annu. Rep. NMR Spectrosc.* **1986**, *17*, 1−78.

(61) de Dios, A. C.; Jameson, C. J. The NMR Chemical Shift: Insight into Structure and Environment. *Annu. Rep. NMR Spectrosc* **1994**, *29* (C), 1−69.

(62) Jameson, C. J. Isotope Effects on Chemical Shifts and Coupling Constants. In *eMagres*; John Wiley & Sons, 2007. .

(63) Jankowski, S. Application of NMR Spectroscopy in Isotope Effects Studies. In *Annual Reports on NMR Spectroscopy*; Elsevier, 2009, Vol. *68*, pp. 149−191. .

(64) Batiz-Hernandez, H.; Bernheim, R. A. Chapter 2 The Isotope Shift. *Prog. Nucl. Magn. Reson. Spectrosc.* **1967**, *3*, 63−85.

(65) Juranić, N. Ligand Field Interpretation of Metal NMR Chemical Shifts in Octahedral d^6 Transition Metal Complexes. *Coord. Chem. Rev.* **1989**, *96*, 253−290.

(66) Juranić, N. Nephelauxetic Effect in Paramagnetic Shielding of Transition-Metal Nuclei in Octahedral d^6 Complexes. *J. Am. Chem. Soc.* **1988**, *110* (25), 8341−8343.

(67) Juranić, N. Nephelauxetic Effect in Metal Ion Paramagnetic Shielding of Spin-Paired d^6 Transition-Metal Complexes. *Inorg. Chem.* **1985**, *24* (10), 1599−1601.

(68) Juranić, N. Significance of Nephelauxetic Effect in the Interpretation of Cobalt-59 Nuclear Magnetic Resonance Frequencies of Cobalt(III) Complex Compounds. *Inorg. Chem.* **1980**, *19* (4), 1093−1095.

(69) Ramsey, N. F. Magnetic Shielding of Nuclei in Molecules. *Phys. Rev.* **1950**, *78* (6), 699−703.

(70) Knetsch, D.; Groeneveld, W. L. Alcohol as Ligands. III.Complexes of Ethylene Glycol with Some Divalent Metal Halides. *Inorg. Chim. Acta* **1973**, *7*, 81−87.

(71) Knetsch, D.; Groeneveld, W. L. Alcohols as Ligands: Part IV. Complexes of Ethylene Glycol with Some Metal(II) Sulfates and Nitrates. *Recl. Des Trav. Chim. Des Pays-Bas.* **1973**, *92* (8), 855−864.

(72) Pico, A. R.; Houk, C. S.; Weakley, T. J. R.; Page, C. J. A New Strontium-Copper Ethylene Glycol Complex: Synthesis and Structure of $[\mathrm{Sr}(\mathrm{C_2H_6O_2})_5][\mathrm{Cu}(\mathrm{C_2H_4O_2})_2]\cdot\mathrm{C_2H_6O_2}$. *Inorg. Chim. Acta* **1997**, *258* (2), 155−160.

(73) Beattie, J. K. Conformational Analysis of Tris-(Ethylenediamine) Complexes. *Acc. Chem. Res.* **1971**, *4* (7), 253−259.

(74) House, I. E.; Tahir, F. M. Deamination of Tris-(Ethylenediamine)Nickel(II) Chloride and Tris(Ethylenediamine)-Platinum(IV) Chloride. *Thermochim. Acta* **1987**, *118* (C), 191−197.

(75) Palmer, J. W.; Stanko, J. A.; Sebti, S. M.; Burdge, J. R. *Mono Ethylenediaminenitroplatinum IV Complexes With Ligands Of Oxides Of Nitrogen As Possible anti-Tumor Agents*; US 5,849,790 A, 1998.

(76) Deferm, C.; Onghena, B.; Nguyen, V. T.; Banerjee, D.; Fransaer, J.; Binnemans, K. Non-Aqueous Solvent Extraction of Indium from an Ethylene Glycol Feed Solution by the Ionic Liquid Cyphos IL 101: Speciation Study and Continuous Counter-Current Process in Mixer−Settlers. *RSC Adv.* **2020**, *10* (41), 24595−24612.

(77) Davis, J. C.; Bühl, M.; Koch, K. R. Probing Isotope Shifts in ^{103}Rh and ^{195}Pt NMR Spectra with Density Functional Theory. *J. Phys. Chem. A* **2013**, *117* (33), 8054−8064.